Received: 5 February 2019 | Revised: 13 June 2019 | Accepted: 17 June 2019

DOI: 10.1111/jmg.12504

ORIGINAL ARTICLE

Journal of METAMORPHIC GEOLOGY | WILEY

On the petrology of brittle precursors of shear zones – An expression of concomitant brittle deformation and fluid–rock interactions in the 'ductile' continental crust?

Thomas Leydier[1] | Philippe Goncalves[1] | Pierre Lanari[2] | Emilien Oliot[3]

[1]UMR6249 CNRS Chrono-Environnement, Université de Franche-Comté, Besançon, France

[2]Institute of Geological Sciences, University of Bern, Bern, Switzerland

[3]Géosciences Montpellier, UMR CNRS 5243, Université de Montpellier, Montpellier, France

Correspondence
Thomas Leydier, Université de Bourgogne-Franche-Comté, UMR6249 Chrono-Environnement, Besançon, France.
Email: thomas.leydier@univ-fcomte.fr

Funding information
Ecole Doctorale Environnement-Santé; Observatoire des Sciences de l'Univers Theta Bourgogne - Franche-Comté program SRO (Soutien à la Recherche de l'Observatoire); Ministère de l'Enseignement Supérieur et de la Recherche; CNRS INSU TelluS-SYSTER 2016

Handling Editor: Richard White

Abstract

The inherited localization model for shear zone development suggests that ductile deformation in the middle and lower continental crust is localized on mechanical anisotropies, like fractures, referred to as shear zone brittle precursors. In the Neves area (Western Tauern Window, Eastern Alps), although the structural control of these brittle precursors on ductile strain localization is well established, the relative timing of the brittle deformation and associated localized fluid flow with respect to ductile deformation remains in most cases a matter of debate. The present petrological study, carried out on a brittle precursor of a shear zone affecting the Neves metagranodiorite, aims to determine whether brittle and ductile deformations are concomitant and therefore relate to the same tectonic event. The brittle precursor consists of a 100–500 μm wide recrystallized zone with a host mineral-controlled stable mineral assemblage composed of plagioclase–garnet–quartz–biotite–zoisite±white mica±pyrite. Plagioclase and garnet preserve an internal compositional zoning interpreted as the fingerprint of Alpine metamorphism and fluid–rock interactions concomitant with the brittle deformation. Phase equilibrium modelling of this garnet-bearing brittle precursor shows that metamorphic garnet and plagioclase both nucleated at 0.6 ± 0.05 GPa, 500 ± 20°C and then grew along a prograde path to 0.75 ± 0.05 GPa, 530 ± 20°C. These amphibolite facies conditions are similar to those inferred from ductile shear zones from the same area, suggesting that both brittle and ductile deformation were active in the ductile realm above 500°C for a depth range between 17 and 21 km. We speculate that the Neves area fulfils most of the required conditions to have hosted slow earthquakes during Alpine continental collision, that is, coupled frictional and viscous deformation under high-fluid pressure conditions ~450°C. Further investigation of this potential geological record is required to demonstrate that slow earthquakes may not be restricted to subduction zones but are also very likely to occur in modern continental collision settings.

KEYWORDS

Alps, brittle precursors, fluid–rock interactions, shear zones, XMapTools

 © 2019 John Wiley & Sons Ltd

1 | INTRODUCTION

Strain localization plays a crucial role in the rheological behaviour of the lithosphere, leading to the development of ductile shear zones above the frictional-viscous transition. Means (1984, 1995) distinguished two main types of shear zones, depending on whether they narrow or widen with time, and raised the question of the recording of the deformation history. Shear zones that narrow with time are excellent time recorders because the margins are progressively deactivated and preserve the early microstructures while strain localizes on the median part due to major softening processes. By contrast, shear zones that widen with time due to either hardening of the shear zone core (Means, 1995) or weakening of the shear zone margins (e.g. Goncalves, Oliot, Marquer, & Connolly, 2012) are not an appropriate time recorder because the entire shear zone remains active during deformation and early microstructures are obliterated by subsequent deformation. In this case, the only way to characterize the mechanical and chemical processes involved is to study immature (short-lived) shear zones that have not experienced significant broadening.

Two end-member models best explain the development of shear zones: inherited localization and dynamic localization models. In both models, strain localization is coeval with significant textural and mineral changes controlling the rheological behaviour of the shear zone. The dynamic localization model involves softening processes due to strain-induced mechanical and chemical changes, like grain size reduction, acquisition of crystallographic preferred orientations and metamorphic/metasomatic reactions (e.g. Gueydan, Leroy, & Jolivet, 2001; Jessell, Bons, Evans, & Piazolo, 2004; Oliot, Goncalves, & Marquer, 2010; Oliot, Goncalves, Schulmann, Marquer, & Lexa, 2014). The inherited localization model implies a pre-existing mechanical or viscosity contrast that concentrates stress and on which ductile strain localizes (e.g. Fusseis & Handy, 2008; Guermani & Pennacchioni, 1998; Mancktelow & Pennacchioni, 2005; Pennacchioni, 2005; Pennacchioni & Mancktelow, 2007; Segall & Pollard, 1983; Segall & Simpson, 1986; Simpson, 1985; Tourigny & Tremblay, 1997; Tremblay & Malo, 1991; Tullis, Dell'Angelo, & Yund, 1990). For instance, shear zones can nucleate on brittle discontinuities (e.g. fractures) affecting the homogeneous protolith, referred to as brittle precursors (e.g. Pennacchioni & Mancktelow, 2007). Nucleation of shear zones along these mechanical discontinuities may be associated with fluid–rock interactions and mineral/chemical changes (Goncalves, Poilvet, Oliot, Trap, & Marquer, 2016).

In the Neves area (Tauern Window, Eastern Alps), field observations on ductile shear zones affecting a metagranodiorite are consistent with the inherited localization model (e.g. Mancktelow & Pennacchioni, 2005; Mancktelow & Pennacchioni, 2013; Pennacchioni & Mancktelow, 2007, 2018). The geometry of the shear zones is structurally controlled by both a network of dykes and dilatant brittle fractures, extending over several tens of metres in length. Along a single fracture, the progressive development of a ductile foliation at 45° from the fracturing plane can be observed, as well as a central suture preserved in the moderate stages of shear zone development (Mancktelow & Pennacchioni, 2005). In this case, ductile deformation localizes directly on the brittle discontinuity. Although the structural control of these brittle precursors on ductile shear zones is very well established in the Neves area, the relative timing of the brittle deformation with respect to the ductile overprinting is still a matter of debate (Fusseis & Handy, 2008; Mancktelow & Pennacchioni, 2005; Segall & Simpson, 1986). To our knowledge, ductile deformation in the Neves area has not been directly dated via radiochronological techniques, but there are several lines of geological evidence supporting an Alpine age (Morteani, 1974; Raith, 1971; Raith, Raase, Kreuzer, & Müller, 1978). The relative timing of the initial brittle deformation is more difficult to establish. Is brittle deformation Alpine in age and closely related to the ductile deformation, or are these two events unrelated and separated in time? If they are unrelated, fractures could correspond to joints inherited from the cooling of the pluton in late Variscan times, then buried and ductilely reactivated during the Alpine orogeny (Pennacchioni & Mancktelow, 2007). On the other hand, fracturing and ductile reactivation could both have occurred at the tertiary Alpine time, under a continuous metamorphic and kinematic regime. Field observations in favour of either Alpine or late Variscan age of the brittle deformation are described thoroughly in Mancktelow and Pennacchioni (2005) and Pennacchioni and Mancktelow (2007) but they are not sufficient to unequivocally refute either of these two hypotheses. One of the goals of this study is to contribute to the debate on the relative timing of brittle and ductile deformation. Constraining the relative timing of both brittle and ductile deformation has not only local and regional implications. If brittle and ductile deformations were coeval and interacting, then it would raise the question of the controlling parameters of deformation style in the middle crust: variation in pore fluid pressure, perturbation in rock viscosity (weakening or hardening) due to fluid–rock interactions and metasomatic reactions, or local stress fluctuations.

Dating brittle deformation is a challenging task and in most cases can be achieved only indirectly, based on structural and/or petrological arguments. In addition, the rock record of frictional deformation and associated fluid flow at great depth is complex to identify because textures related to the transient brittle deformation events and fluid flow tend to be overprinted by the long-lasting viscous deformation events and retrogressed during exhumation. Nonetheless, petrological and micro-textural studies have been successfully conducted on natural exhumed shear zones that have recorded concomitant frictional and viscous deformation with fluid flow. Among them, Goncalves et al. (2016) and Angiboust et al. (2015) have been able to demonstrate that viscous and frictional deformation observed in shear zones were coeval and related to the same event or at least to the same *P*–*T* conditions, based on the presence of syn-kinematic and/or synmetamorphic fluid percolation phases suitable for thermobarometric analyses.

In the case of the Neves area, it is critical to study brittle fractures with very limited or no overprinting, which could have obliterated all the features related to the brittle stage. We have, therefore, conducted a petrological analysis on a discrete brittle fracture. This fracture is inferred to be equivalent to brittle precursors of shear zones. The approach followed in this contribution consists of detailed petrographical observations combined with high-resolution quantitative compositional mapping to highlight the texture and mineral assemblages related to brittle deformation and associated fluid flow. Thermodynamic modelling on local assemblages was applied to retrieve the *P*–*T*–fluid conditions under which the brittle precursor of shear zones formed. Then, the crucial role of metasomatism in the frictional–viscous interactions during shear zone nucleation is discussed.

2 | NEVES AREA AND STUDIED OUTCROP

The Neves area is located within the subpenninic units exposed at the southwestern part of the Tauern tectonic window (Figure 1a), consisting of a Variscan basement intruded by Permo-Carboniferous magmatic intrusions (*c*. 290–310 Ma) and a metasedimentary cover (Figure 1b) (Frisch, 1980; Kurz, Neubauer, & Genser, 1996; Kurz, Neubauer, Genser, & Dachs, 1998; Schmid, Scharf, Handy, & Rosenberg, 2013). As a result of the Alpine Barrovian metamorphism that affected the Tauern Window during the Oligocene (Schmid et al., 2013), these units reached amphibolite facies conditions with a thermal peak of 550–600°C (isograds on Figure 1b) and 0.5–0.7 GPa, at *c*. 28–30 Ma (Christensen, Selverstone, Rosenfeld, & DePaolo, 1994; Inger & Cliff, 1994; Reddy, Cliff, & East, 1993). The metasediments were pervasively mylonitized by an alpine ductile deformation occurring under amphibolite facies conditions. It resulted in a large mylonite zone embedding the weakly affected magmatic intrusions, in which strain localized in numerous mainly east–west trending ductile shear zones, with a width ranging from a few tens of mm to a few metres (De Vecchi & Mezzacasa, 1986; Glodny, Ring, & Kühn, 2008; Morteani, 1974; Pennacchioni & Mancktelow, 2007; Steffen & Selverstone, 2006). This low-strain plutonic domain is referred to as Zentralgneise (Morteani, 1974). The studied outcrop is located in the southwestern part of the Zentralgneise, 4 km northeast of the Neves lake in the South Tyrol, Italy. This outcrop corresponds to a large and glacier-polished area of several hundred square metres located at the front of the rapidly retreating Mesule glacier. Mancktelow and Pennacchioni (2005) and Pennacchioni and Mancktelow (2007) have performed a detailed structural analysis of this area. We will summarize here the main results relevant for this contribution.

The late Variscan metagranodiorite is affected by thin and straight brittle fractures ranging from several tens to hundreds of metres in length (Figure 2a). Different sets of sub-vertical fractures can be distinguished depending on their orientation, but the predominant set is oriented approximately east–west. These fractures can either be isolated or arranged in networks with a low-angle en-échelon geometry with a left-stepping pattern (Figure 2b,c; see also fig. 5 in Mancktelow & Pennacchioni, 2005; and fig. 3a in Pennacchioni & Mancktelow, 2007). At a smaller scale and in most cases, a single fracture does not show any apparent offset but when present, the offset, of a few centimetres, is dextral and consistent with the en-échelon geometry previously described (see fig. 3 in Mancktelow & Pennacchioni, 2005). Fractures are commonly highlighted by a thin biotite-rich layer and by aligned rust stains scattered along the fracture, consistent with the presence of sulphide. In response to metamorphic fluid infiltrations, the fractures can also be filled by epidote, and the surrounding metagranodiorite is very commonly altered, resulting in bleached haloes developed on both sides of the central epidote-rich vein. These alteration haloes differ from the surrounding metagranodiorite by the frequent presence of calcite, and coarse grains of poikilitic Ca-rich plagioclase, containing inclusions of quartz±biotite±calcite (Mancktelow & Pennacchioni, 2005).

Ductile shear zones show a strong spatial relationship with these pre-existing structures, suggesting that the nucleation of shear zones is controlled by them. Ductile deformation can either localize directly on the biotite-rich fractures, producing single ductile shear zones (Figure 2d–f), or flank the bleached haloes, resulting in a characteristic paired ductile shear zone (Figure 2g). Mesoscale field observations have been used by Mancktelow and Pennacchioni (2005) to demonstrate that these fractures are the brittle precursors of single ductile shear zones. The ductile overprinting is characterized by the progressive development of a straight foliation defined by elongated biotite, over a width of 1–2 cm on both sides of the fracture and oriented at 45° to it, which evolves with the widening of the shear zone into a sigmoidal foliation (Figure 2e,f). This widening stage can result in up to 1 or 2 m wide shear zones. A single fracture can show the longitudinal and gradational transition, from a joint without any offset to a few

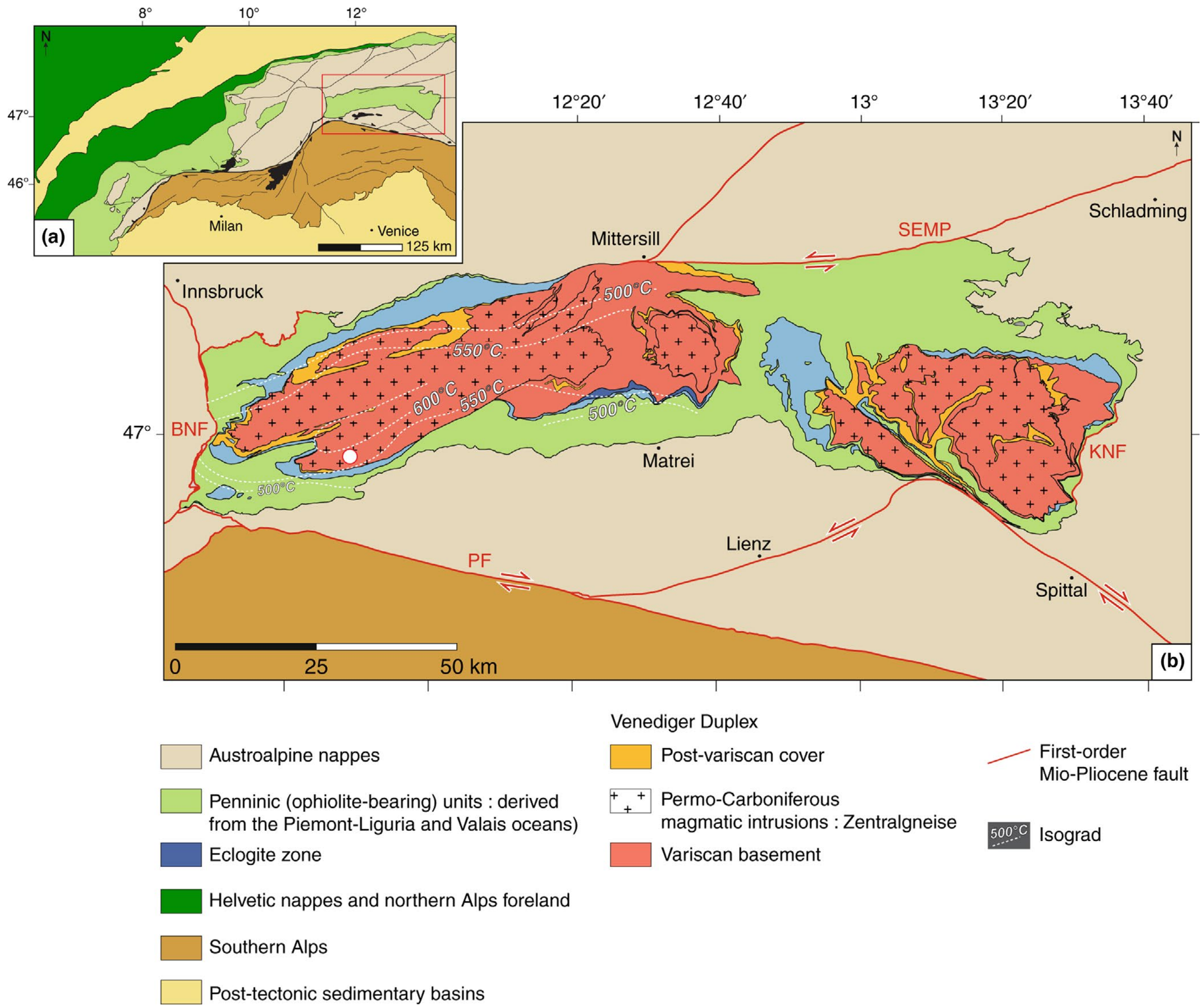

FIGURE 1 (a) Simplified tectonic map of the Alps. The red box indicates the location of (b). (b) Simplified tectono-metamorphic map of the Tauern Window (Eastern Alps). Only the subpenninic units are differentiated, the Austroalpine nappes are not detailed. The white circle indicates the location of the Neves area. The dashed lines represent the isograds of the alpine metamorphism in the western Tauern Window (after Hoernes & Friedrichsen, 1974). The abbreviations for the main Mesozoic fault systems are: BNF, Brenner Normal Fault; KNF, Katschberg Fault System; PF, Periadriatic Fault system; SEMP, Salzach–Ennstal–Mariazell–Puchberg system. Map modified after Pennacchioni and Mancktelow (2007) and Schmid et al. (2013)

centimetres wide ductile shear zone. The kinematics of the east–west ductile shear zones is mostly dextral, which is consistent with offsets of brittle fractures.

This contribution is primarily focused on the brittle precursors of single ductile shear zones, and aims to characterize texture, mineralogy, and fluid–rock interactions related to the early brittle deformation. Therefore, the strategy was to focus on brittle precursors without evidence of any ductile reactivation. Sampling such discrete brittle fractures is particularly challenging, because most samples are likely to split along this weakness. The studied sample contains a healed fracture crosscutting the metagranodiorite without any offset in either

FIGURE 2 (a) Brittle fractures showing a left-stepping en-échelon pattern, extending to several tens of metres in length, highlighted by the alignment of rust stains, attesting to the presence of pyrite (looking west, 46°58′32.4″, 11°48′01.7″). The black box indicates the location of (b). (b) Zoom on the left-stepping en-échelon geometry. (c) Compressive bridge between left-handed en-échelon brittle fractures (looking west, 46°58′25.0″, 11°47′48.9″). (d) Biotite-rich brittle precursor (e) upon which localizes an incipient ductile deformation with a discrete foliation oriented at ~45° from the initial fracture, leading to the development of (f) a single ductile shear zone. (g) Epidote-rich vein surrounded by a bleached halo, on the edges of which localizes a paired ductile shear zone

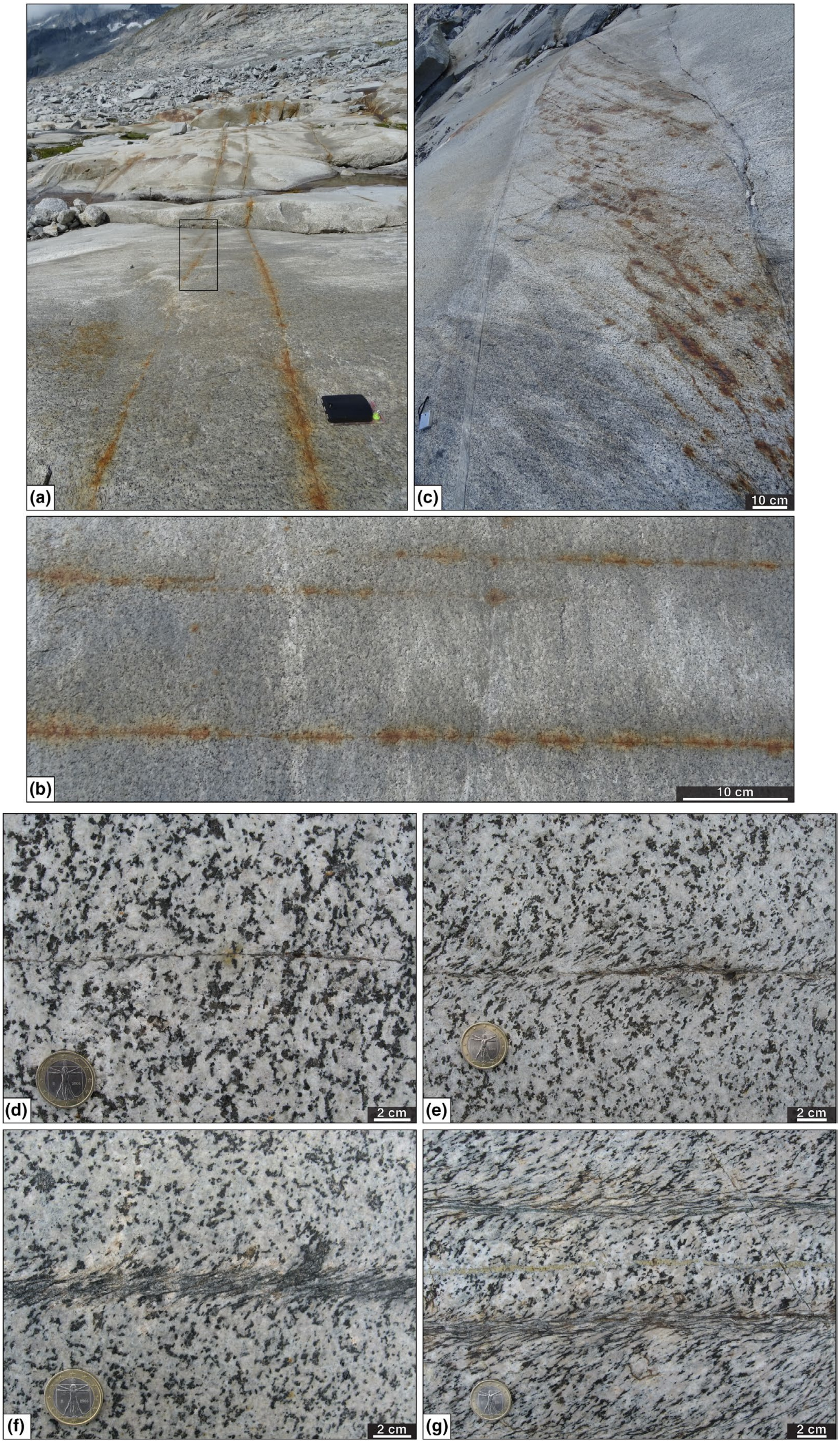
(a)
(c)
10 cm
(b)
10 cm
(d)
2 cm
(e)
2 cm
(f)
2 cm
(g)
2 cm

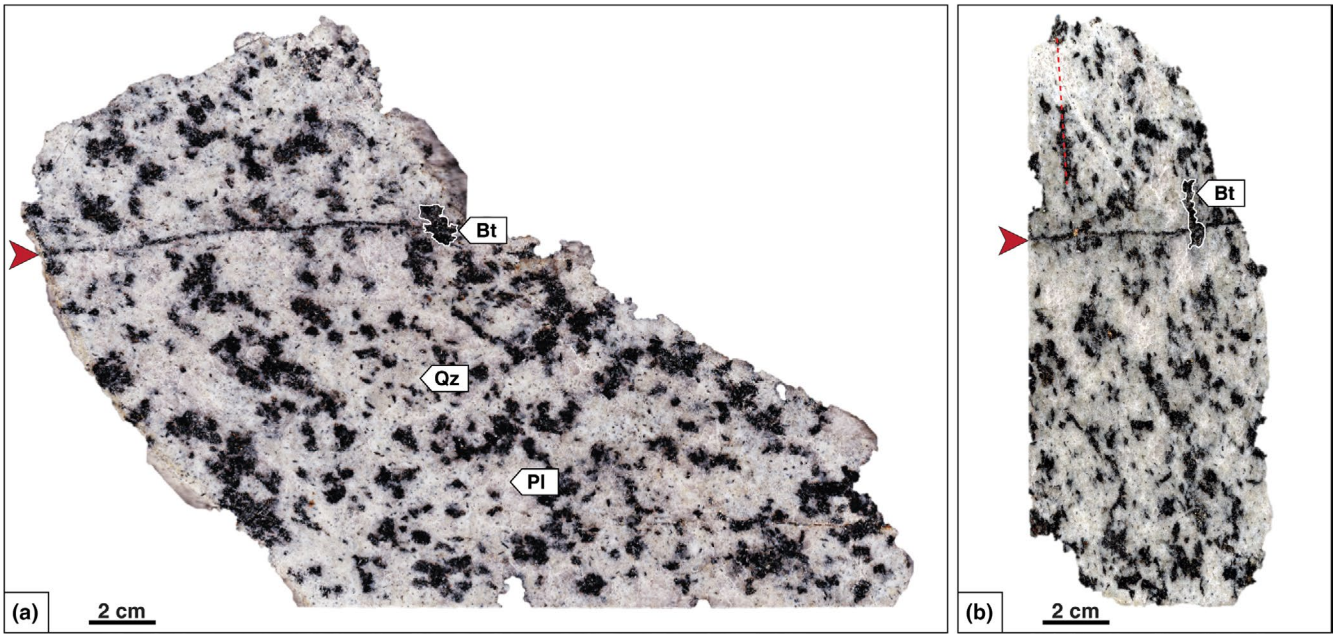

FIGURE 3 (a) and (b) Two perpendicular sections of the same sample of the undeformed metagranodiorite crosscut by an immature shear zone precursor. The location of the fracture is indicated by the red arrows. The outlined biotite aggregates highlight the absence of offset along the fracture. In (b), the biotite aggregates materialize a rough magmatic foliation (dotted red line)

macroscopic ductile overprint (Figure 3). On the sample scale, the knife-sharp pattern of the fracture is highlighted by a biotite trail.

3 | CONTROL OF THE HOST ROCK ON THE BRITTLE PRECURSOR MINERALOGY

The mineralogy of the brittle precursor was characterized using optical microscopy coupled with a cathodoluminescence (CL) cold cathode operated at 15.5 ± 0.3 keV and 483 ± 11 mA, backscattered electron imaging and high-resolution X-ray mapping. CL imaging allows the main phases (quartz, feldspars, and biotite) to be distinguished and highlights the variations in Na/Ca ratio in plagioclase (Oliot et al., 2010). High-resolution X-ray maps have been acquired using a JEOL-8200 microprobe at the Institute of Geological Sciences (University of Bern). Operating conditions were 15 keV, 100 nA, with a pixel resolution of 1 μm and a dwell-time of 100 ms/pixel. A standardization step is required in order to convert measured X-ray intensities (photon counts per pixel) into oxide weight per cent concentrations. For each phase, an average of 10 spot analyses were acquired along several transects, at high angle from the grain boundaries, to take into account the mineral heterogeneities. These spot analyses were used as internal standards to obtain the quantified maps (element concentration or phase component proportion), using the software solution XMapTools 2.4.3 (Lanari, Vho, Bovay, Airaghi, & Centrella, 2018; Lanari et al., 2014). The mineral abbreviations used below are from Whitney and Evans (2010).

3.1 | Undeformed metagranodiorite

The undeformed metagranodiorite was used as a reference frame to define the metamorphic/metasomatic reactions involved in the discrete brittle precursor. It is composed of quartz, plagioclase, biotite, ±K-feldspar, ±white mica, and ±epidote. The undeformed protolith is rather homogeneous, and mainly consists in the juxtaposition of large quartz, plagioclase, and biotite aggregates defining a magmatic foliation (Figure 4), as described by Mancktelow and Pennacchioni (2005).

Quartz (Qz, ~20 vol.%) occurs as 500 μm–1 mm diameter grains clustered in large irregular aggregates. These grains present a weak undulose extinction and are irregular, serrated to lobate boundaries. Igneous calcic plagioclase (Pl_i) underwent saussuritization, producing epidote (Ep_0), white mica (Wm), and ±biotite, which mainly occur as randomly oriented small grains (a few tens to a few hundreds of micrometres in length) scattered within the host crystal. Although these coarse grains of more albitic saussuritized plagioclase (Pl_0) are locally preserved, they are extensively recrystallized into finer grained (100–300 μm in diameter) aggregates (50 vol.%). Numerous grains of epidote, white mica, and ±biotite are still present within these recrystallized aggregates. Within the plagioclase aggregates, the inter-granular volume is filled with anhedral K-feldspar (Kfs, <10 vol.%) highlighting the original shape of plagioclase grains. K-feldspar can also be found as small grains aggregates spread within the quartz-rich domains (Figure

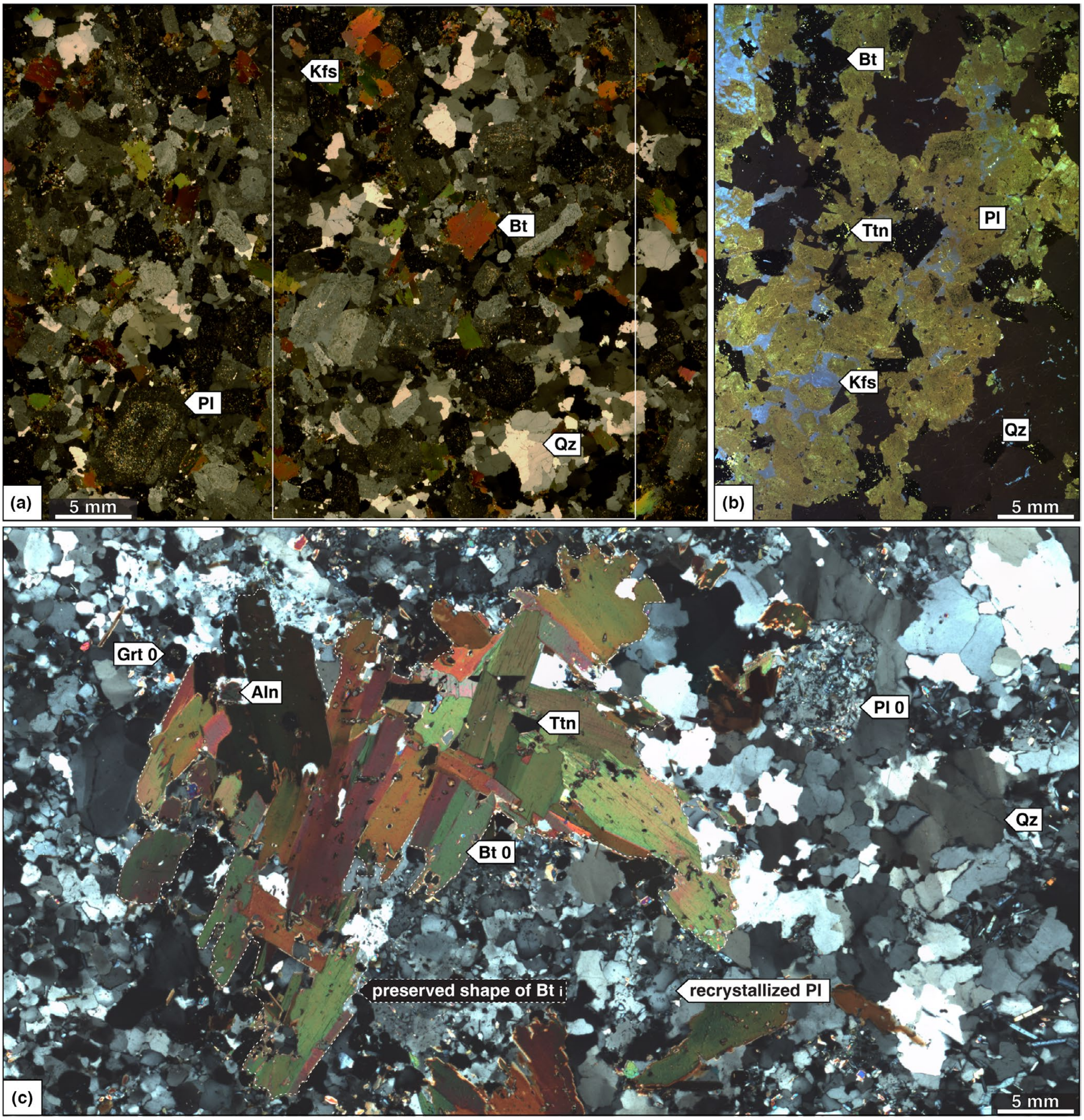

FIGURE 4 (a) Cross-polarized thin section scan, (b) cathodoluminescence (CL) image and (c) cross-polarized photomicrograph of the undeformed metagranodiorite. The white box in (a) indicates the location of (b). The preserved shape of the former magmatic biotite (Bt_i), recrystallized in Bt_0, is outlined by the white dotted line. Aln, allanite; Bt, biotite; Grt, garnet; Pl, plagioclase; Qz, quartz; Ttn, titanite

4b,c). Magmatic biotite (Bt_i) defining the magmatic foliation is largely replaced by aggregates of recrystallized smaller grains (Bt_0, up to 1 mm in length, 20 vol.%). Numerous titanite (Ttn) inclusions are observed (Figure 4b). Garnet of irregular shape (Grt_0, 100–200 μm), with cores containing numerous quartz and plagioclase inclusions, form a discontinuous coronitic rim around the recrystallized biotite Bt_I. Prismatic grains of allanite (Aln), surrounded by an epidote rim, are locally preserved.

3.2 | Mineralogical variability in the precursor

The brittle precursor is sealed by a 100–500 μm wide zone of recrystallized minerals. In contrast to the knife-sharp aspect of precursors at both outcrop and sample scales (Figures 2a,b and 3), this recrystallized zone shows quite irregular boundaries at the thin-section scale (Figure 5). No offset is observed

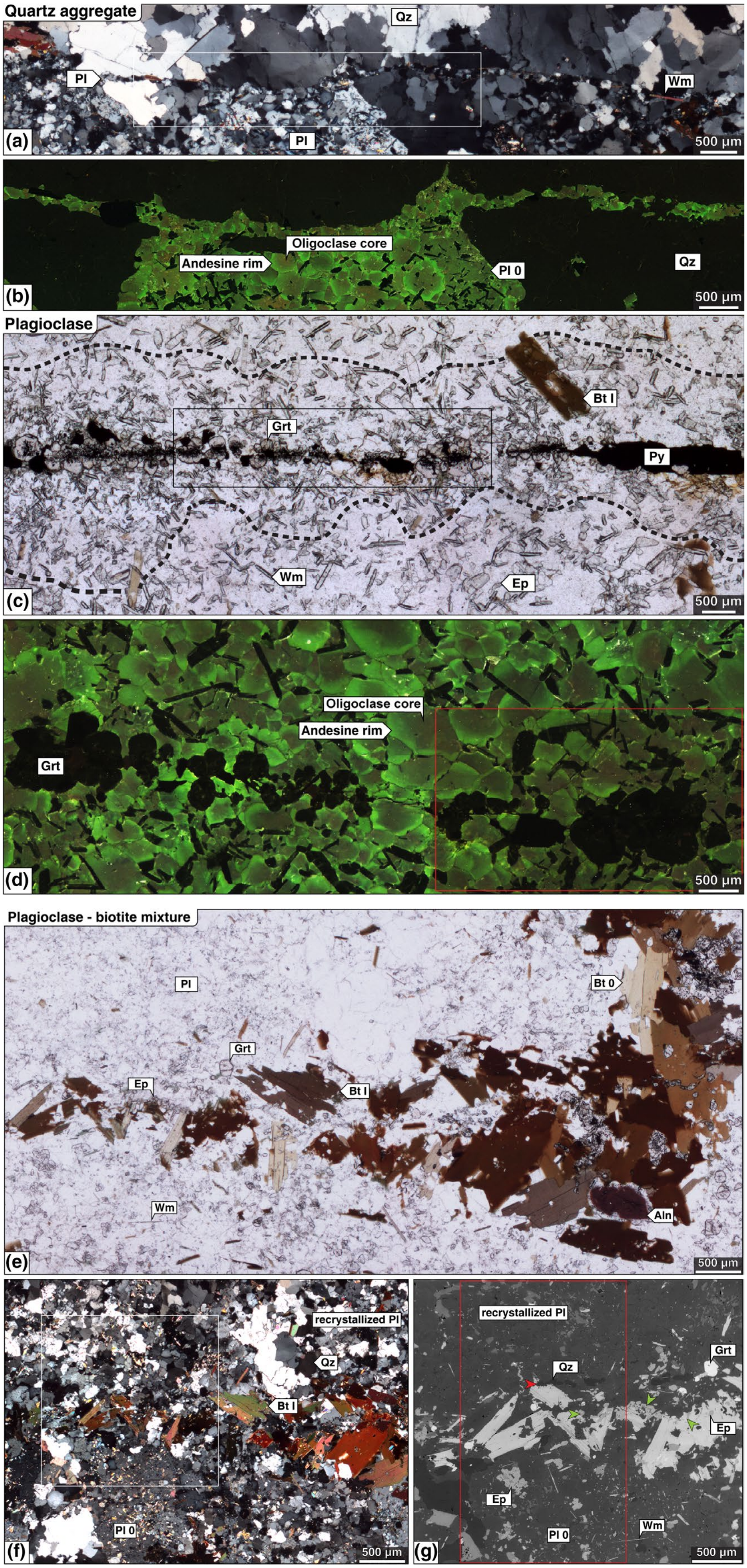

FIGURE 5 (a) Photomicrograph and (b) cathodoluminescence (CL) image of the brittle precursor through a quartz aggregate. The pattern of the precursor is outlined by the newly formed plagioclase. The white box in (a) indicates the location of (b). (b) CL colour highlights the chemical zoning in recrystallized metamorphic plagioclase, with oligoclase-rich cores surrounded by andesine thin rims (reddish and greenish CL colour, respectively). (c) Photomicrograph and (d) CL image of the brittle precursor through plagioclase. Dotted black lines in (c) materialize the area, around the garnet and pyrite alignment, in which modal amounts of epidote and white mica are more important. The black box in (c) indicates the location of (d). The red box in (d) indicates the location of the X-ray map (Figure 6b,d,e). (e) Photomicrograph and (f) cross-polarized photomicrograph of the brittle precursor in a plagioclase–biotite (Bt_0) mixture. Newly formed biotite (Bt_I) materializes the brittle precursor pattern, as do the numerous epidote inclusions (Ep). White box in (f) indicates the location of (g). (g) BSE image of the biotite-rich precursor. The red and green arrows outline the newly formed quartz and epidote alignments, respectively. The red box indicates the location of the X-ray map (Figure 6a)

along the fracture at this scale. Three distinct metamorphic assemblages are visible within the precursor, controlled by the host mineral or assemblage truncated by the fracture.

Where the brittle precursor cuts a quartz aggregate (Figure 5a,b) it forms a 80–100 μm wide domain that consists mostly of recrystallized plagioclase grains of 40–100 μm in size with minor epidote. Both within or outside the precursor, newly formed plagioclase shows intragranular variations in CL, attesting for variations in composition, with Na-rich cores (enriched in oligoclase) surrounded by thin Ca-enriched (andesine) rims (reddish and green CL colour, respectively, in Figure 5b). Fracture boundaries are locally underlined by 100–300 μm long aligned grains of white mica.

Within the large saussuritized plagioclase grain (Figure 5c,d), the precursor is defined by an alignment of small aggregates of euhedral garnet (<50 μm in diameter) and pyrite (Py). Similar textures in mm-scale mylonites have been described by White and Clarke (1994). Garnet cores contain numerous quartz and pyrite inclusions aligned parallel to the precursor. The saussuritized plagioclase Pl_0 is recrystallized into a polymineralic and polygonal aggregate of newly formed metamorphic plagioclase, with euhedral epidote and white mica. The recrystallized zone is characterized by a larger modal amount of epidote and white mica (Figure 5c). In CL, the recrystallized plagioclase shows the same zoning feature as previously described in quartz aggregate: an oligoclase-rich core surrounded by an andesine-rich rim (Figure 5d).

In domains consisting of a mixture of former magmatic plagioclase and biotite (Figure 5e–g), the precursor consists of newly formed biotite (Bt_I), epidote, recrystallized plagioclase, and isolated small euhedral garnet grains. Biotite forms crystals up to 150–300 μm in length concentrated along the brittle precursor with an orientation subparallel to slightly oblique with respect to the fracture direction. Epidote occurs as small rounded to elongated grains (<60 μm) either in the matrix or in Bt_I, where they form inclusion trails interpreted as the location of the initial fracture. Plagioclase consists of an aggregate of recrystallized and zoned plagioclase with locally aligned small newly formed quartz grains. Small euhedral garnet, containing quartz and pyrite inclusions in their core, are scattered along the precursor.

3.3 | Mineral chemistry

Along the precursor, although the mineral assemblage and proportions varies depending on the host magmatic mineral (quartz, plagioclase, and biotite), the chemical composition of the newly formed phases is very consistent. Average representative compositions are reported in Table 1. The SDs correspond to one sigma relative uncertainties. The precursor local assemblages, as well as the abbreviations of the different generations, for each phase, are summarized in Table 2.

Metamorphic biotite aggregated in the undeformed protolith (Bt_0) and biotite aligned along the precursor (Bt_I), have the same composition with X_{Mg} (=Mg/(Mg+Fe); with Fe and Mg in atom per formula unit, *apfu*) of 0.38 ± 0.01 and 0.37 ± 0.02 for Bt_0 and Bt_I, respectively. By contrast, the composition of the magmatic Bt_i relicts has a higher titanium *apfu* (0.17 vs. 0.15 and 0.13, for $Bt_{i,\ 0\ \mathrm{and}\ I}$, respectively). X_{Mg} in Bt_i is also lower (0.33 ± 0.01). Epidote compositions in the precursor and in the undeformed protolith are very similar: they both exhibit the same zoisite fraction of Zo_{52-54}.

Three generations of plagioclase have been texturally and compositionally defined. The compositional maps of Figure 6 show the molar proportion of albite in plagioclase (X_{Ab}) located in the biotite-rich (Figure 6a,c) and garnet-rich precursor (Figure 6b). Plagioclase Pl_0, corresponding to a large relict of saussuritized plagioclase visible on the lower part of Figure 6a, exhibits a distinct mottled texture with a composition ranging from of Ab_{75} to Ab_{80}. By contrast, recrystallized aggregates of plagioclase show a smoother variation in composition (Figure 6a–c). Recrystallized plagioclase shows an inverse compositional zoning, as expected from CL imaging, with cores (referred to as Pl_I) characterized by the highest albite content (Ab_{80-82}) while the thin rims, defined as Pl_{II}, show the lowest Ab content (Ab_{60-75}). The compositional maps also reveal two distinct styles of transition between Pl_I and Pl_{II}, with Pl_I domains that either evolve gradually to Pl_{II} compositions or are alternatively sharply truncated by Pl_{II} domains, resulting in grains with truncated Pl_I 'cores', offset with respect to the centre of the mineral (Figure 6c, see dotted line and arrows). Such a texture suggests a dissolution–precipitation mechanism, with distinct *P*–*T*–fluid conditions between Pl_I and Pl_{II}. Figure 6a also reveals that (a) Pl_{II} is significantly more abundant in the ~300 μm wide precursor, where Bt_I and epidote are observed and (b) Pl_{II} also defines thin irregular stripes running across the former saussuritized Pl_0. This structure is interpreted as a former fracture formed at a high angle to the main brittle precursor. Finally, the compositional map of the garnet-bearing precursor, developed in a large Pl_0, also shows that Pl_{II} is more abundant when plagioclase is in direct contact with the aligned garnet (Figure 6b). All these textures suggest that Pl_{II}, and at least garnet rims, are very likely related to inter-granular percolation of fluids along and across the brittle precursor.

Aligned garnet along the garnet-rich precursor and isolated euhedral garnet within the biotite-rich precursor were also analysed. Figure 6d,e shows the molar proportions of spessartine (X_{Sps}) and grossular (X_{Grs}) in garnet. Each grain exhibits a core-to-rim compositional zoning. Garnet cores (Grt_I), which contain quartz and sulphide inclusions, are characterized by the highest spessartine and lowest grossular content, with a composition of Sps_{06-09} and Grs_{25-27}. Within the aggregate of smaller garnet (left side of the map, Figure 6d),

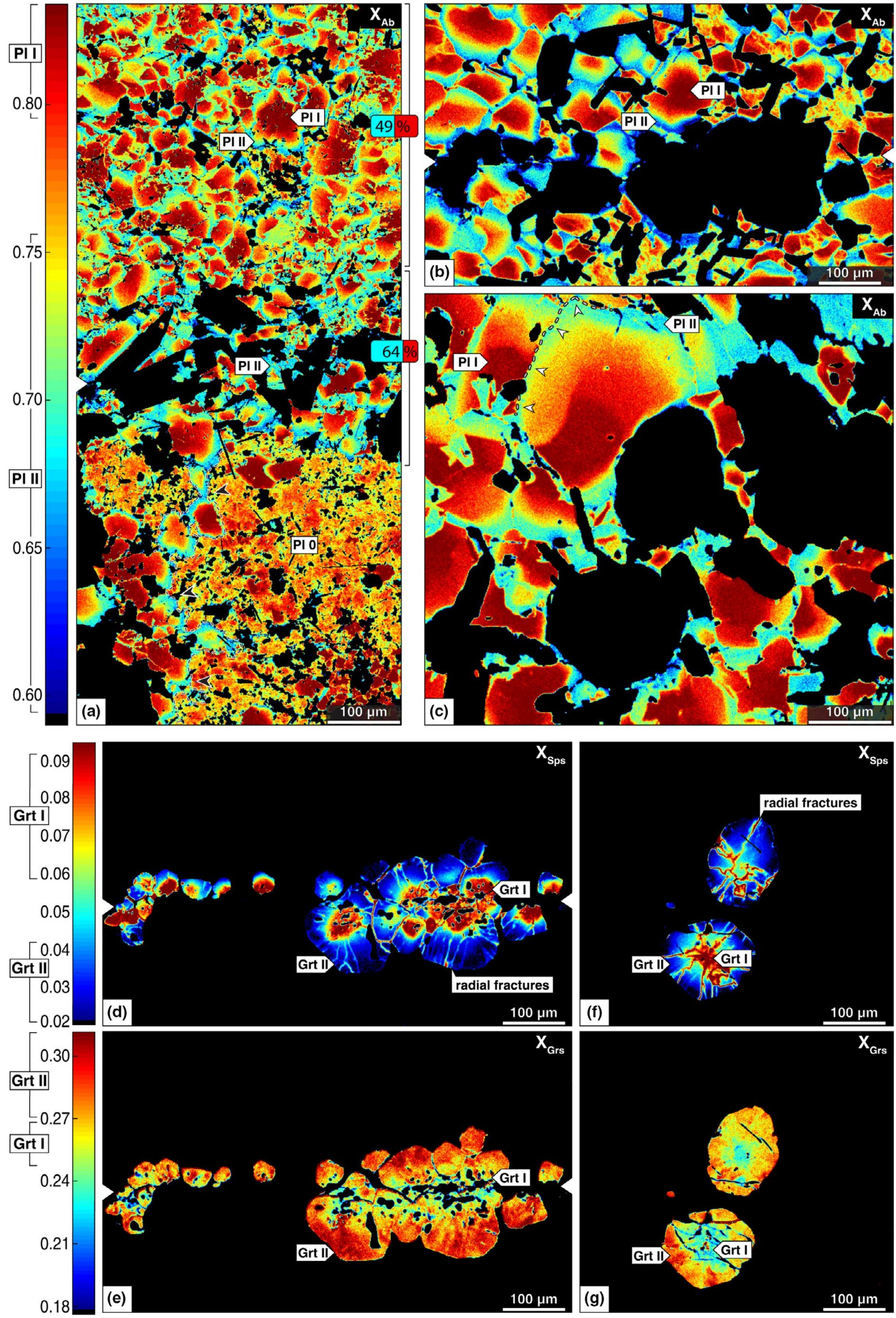
X_Ab
Pl I
Pl II
Pl 0
49 %
64 %
0.80
0.75
0.70
0.65
0.60
(a)
(b)
(c)
100 µm
X_Sps
X_Grs
Grt I
Grt II
radial fractures
0.09
0.08
0.07
0.06
0.05
0.04
0.03
0.02
0.30
0.27
0.24
0.21
0.18
(d)
(e)
(f)
(g)

FIGURE 6 Quantitative X-ray maps exhibiting the albite content (X_{Ab} = Na/(Na + Ca)) in plagioclase. Only plagioclase is coloured (albite content increases from blue to red), other phases are in black. (a) X-ray map centred and processed on the biotite-rich precursor (see Figure 5d). The black dotted lines and the grey arrows outline the pattern of a former fracture formed in the saussuritized magmatic plagioclase (Pl0), filled by Pl_{II}. On the right side, the percentage values in the two boxes indicate the proportions of Pl_{II} (light blue) with respect to Pl_I (red), along the precursor and in the surrounding plagioclase aggregate. (b) X-ray maps processed on the garnet-bearing precursor (see Figure 5b). White arrows on the borders of (a) and (b) materialize the location of the brittle precursor. (c) X-ray maps processed close to the biotite-bearing precursor, showing isolated garnet (uncoloured minerals in the centre of the map) surrounded by recrystallized metamorphic plagioclase. The white dotted line and arrows highlight a sharp boundary between a Pl_I truncated core (on the left) and the later Pl_{II} rim of the neighbour grain (on the right). Quantitative X-ray maps exhibiting the spessartine (d, f) and grossular (e, g) contents (X_{Sps}=Mn/(Fe+Ca+Mg+Mn), X_{Grs}=Ca/(Fe+Ca+Mg+Mn)) in garnet. Only garnet is coloured (spessartine and grossular contents increase from blue to red), other phases are in black. (d, e) X-ray maps processed on the garnet-bearing precursor (same area as Figure 6b). White arrows on the borders of (d) and (e) materialize the location of the brittle precursor. (f, g) X-ray maps processed close to the biotite-bearing precursor, showing isolated garnet surrounded by recrystallized plagioclase (here in black, see Figure 6c)

spessartine-rich core (Sps_{07}, Grs_{25}) occurs as elongated nucleus parallel to the precursor. The inclusion-free rim (Grt_{II}) has a slightly different composition with a gently and continuous decrease in spessartine content from 4 to 2%. Rims are crosscut by healed radial fractures that connect the matrix to the spessartine-rich core. Compositions of healed garnet along the fractures are characterized by an intermediate spessartine content ranging from 3 to 6%. Isolated euhedral garnet in the biotite-bearing precursor show the same pattern (Figure 6f–g). However, Grt_I does not contain any pyrite and quartz inclusions. We suggest that the aligned sulphide and quartz are characteristics of fluid circulation within the brittle precursor that were captured during garnet growth.

In conclusion, two distinct metamorphic stages are defined. For stage 1, we assume that plagioclase cores (Pl_I) were in equilibrium with garnet cores (Grt_I). Stage 2 corresponds to the equilibrium conditions of plagioclase rims (Pl_{II}) with garnet rims (Grt_{II}). Most of the epidote grains are located at the grain boundaries. Epidote is more likely related to stage 2, and was labelled as Ep_{II}.

4 | *P–T* ESTIMATES OF THE VARIOUS METAMORPHIC STAGES

Pseudosections (isochemical phase diagrams) have been computed to constrain the *P–T* conditions of crystallization of the local equilibria in the precursors and associated with the fluid circulations related to the brittle deformation. Phase relations have been modelled in the system MnO–Na_2O–CaO–K_2O–FeO–Fe_2O_3–MgO–Al_2O_3–SiO_2–H_2O, with Perple_X 6.6.8 (Connolly, 1990, 2005; Connolly & Kerrick, 1987) and the thermodynamic database of Holland and Powell (2011). Solution models and end-member phases considered in the modelling are listed in Table 3. Field observations provided by Mancktelow and Pennacchioni (2005) and Pennacchioni and Mancktelow (2007), added to our petrographical observations (e.g. recrystallized plagioclase along the main fracture and along discrete zones at high angle to it), suggest that brittle deformation was accompanied by fluid percolation. Therefore, thermodynamic modelling was performed under fluid-saturated conditions. Fluid is assumed to be pure H_2O for simplification. The oxidation state (Fe_2O_3/FeO) of stages 1 and 2 was estimated using $T-X_{Fe_2O_3}$ sections at a fixed pressure of 0.6 and 0.7 GPa, respectively. This estimation was constrained based on the mineral assemblage and garnet compositions.

4.1 | Reactive bulk composition

The challenge is to determine accurately the equilibrium volume and the associated reactive bulk composition to model phase relations as the studied sample is characterized by strongly zoned minerals (mostly a core-rim zoning in plagioclase and garnet). These preserved cores imply that parts of minerals were removed from the reacting part of the rock volume (Lanari & Engi, 2017; Spear, 1988; Stüwe, 1997). Therefore, a relevant reactive bulk composition has to be estimated for each stage to be modelled. Molar local bulk compositions were extracted from the quantitative maps using the functions available in XMapTools (Lanari & Engi, 2017; Lanari et al., 2018). This software allows the user to select only the relevant minerals (composition and modes) of a region of interest. Pseudosections are here based on the quantitative maps performed on the plagioclase and garnet-rich precursor (Figure 6b,d,e), then compositions of both phases can be used to constrain the *P–T* conditions of stages 1 and 2. The reactive bulk compositions are shown in Figure 7 and compared with the undeformed granodiorite composition, the composition of the saussuritized plagioclase Pl_0 and a theoretical magmatic plagioclase composition expected in a granodiorite (andesine $Na_{0.6}Ca_{0.4}Al_{1.4}Si_{2.6}O_8$) where the garnet-plagioclase assemblage is developed (Figure 5c,d). Figure 7 shows that the bulk compositions obtained for stages 1 and 2 significantly differ from the magmatic plagioclase compositions, and rather reflect the composition of the metagranodiorite, suggesting a behaviour similar to a closed system during deformation and metamorphism. As expected, stage 2 reactive bulk composition is more calcic than for the stage 1 (Figure 7).

TABLE 1 Average composition of plagioclase, biotite, garnet, and epidote in the undeformed metagranodiorite (Pl_0, $Bt_{i, 0}$, Grt0, and Ep0) and along the brittle precursor ($Pl_{I, II}$, Bt_I, $Grt_{I, II}$, and Ep_{II})

	Plagioclase				**Biotite**		
	Pl_0 (N = 4)	**Pl_I (N = 27)**	**Pl_{II} (N = 24)**		**Bt_i (N = 13)**	**Bt_0 (N = 14)**	**Bt_I (N = 28)**
wt% oxyde							
SiO_2	62.32 ± 0.67	63.74 ± 1.18	62.59 ± 1.54		35.43 ± 0.24	35.99 ± 0.66	35.63 ± 0.77
TiO_2	—	—	—		2.92 ± 0.10	2.62 ± 0.13	2.16 ± 0.30
Al_2O_3	21.85 ± 0.66	22.22 ± 0.86	23.14 ± 0.86		16.48 ± 0.28	16.93 ± 0.19	16.89 ± 0.38
FeO	0.04 ± 0.03	0.11 ± 0.05	0.01 ± 0.04		23.52 ± 0.38	22.70 ± 0.25	23.26 ± 0.91
MnO	—	—	—		0.35 ± 0.04	0.29 ± 0.01	0.31 ± 0.05
MgO	0.00	0.00	0.00		6.37 ± 0.16	7.69 ± 0.23	7.62 ± 0.43
CaO	4.11 ± 0.69	3.89 ± 0.77	4.77 ± 0.91		0.01 ± 0.02	0.02 ± 0.02	0.04 ± 0.04
Na_2O	9.17 ± 0.37	9.38 ± 0.43	8.82 ± 0.52		0.10 ± 0.02	0.09 ± 0.04	0.11 ± 0.04
K_2O	0.17 ± 0.05	0.21 ± 0.04	0.19 ± 0.06		9.53 ± 0.12	9.16 ± 0.15	8.87 ± 0.47
Total	97.95 ± 0.35	99.73 ± 1.25	99.85 ± 1.43		95.36 ± 0.26	95.51 ± 1.03	94.98 ± 0.86
Formula 8(O)							
Si	2.85 ± 0.03	2.85 ± 0.02	2.77 ± 0.03		2.78 ± 0.01	2.78 ± 0.02	2.77 ± 0.04
Ti	—	—	—		0.17 ± 0.01	0.15 ± 0.01	0.13 ± 0.02
Al	1.16 ± 0.03	1.14 ± 0.02	1.22 ± 0.03		1.52 ± 0.02	1.54 ± 0.02	1.55 ± 0.04
Fe	0.00	0.00	0.00		1.54 ± 0.03	1.47 ± 0.02	1.51 ± 0.06
Mn	—	—	—		0.02 ± 0.01	0.02 ± 0.01	0.02 ± 0.01
Mg	0.00	0.00	0.00		0.74 ± 0.02	0.89 ± 0.03	0.88 ± 0.05
Ca	0.20 ± 0.03	0.16 ± 0.02	0.24 ± 0.03		0.00	0.00	0.00
Na	0.80 ± 0.03	0.83 ± 0.03	0.75 ± 0.03		0.01 ± 0.00	0.01 ± 0.01	0.02 ± 0.01
K	0.01 ± 0.01	0.01 ± 0.01	0.01 ± 0.01		0.95 ± 0.01	0.90 ± 0.01	0.88 ± 0.04
Total	5.01 ± 0.01	5.00 ± 0.01	5.00 ± 0.01		7.77 ± 0.02	7.76 ± 0.02	7.77 ± 0.03
Ab molar	0.79 ± 0.03	0.82 ± 0.02	0.75 ± 0.03	$X_{Mg\ molar}$	0.33 ± 0.01	0.38 ± 0.01	0.37 ± 0.02

	Garnet					**Epidote**	
	Grt_0 (cores) (N = 2)	**Grt_0 (rims) (N = 4)**	**Grt_I (N = 5)**	**Grt_{II} (N = 10)**		**Ep_0 (N = 4)**	**Ep_{II} (N = 11)**
wt% oxyde					wt% oxyde		
SiO_2	37.19 ± 0.37	37.57 ± 0.42	36.78 ± 0.55	37.20 ± 0.64	SiO_2	39.62 ± 0.12	39.37 ± 0.66
TiO_2	0.30 ± 0.06	0.10 ± 0.05	0.03 ± 0.03	0.04 ± 0.03	TiO_2	0.08 ± 0.07	0.05 ± 0.06
Al_2O_3	21.55 ± 0.18	21.73 ± 0.03	21.63 ± 0.25	21.62 ± 0.06	Al_2O_3	27.83 ± 0.40	27.45 ± 0.38
FeO	27.68 ± 0.69	29.34 ± 0.54	29.63 ± 1.08	29.23 ± 0.88	Fe_2O_3	8.01 ± 0.57	8.17 ± 0.22
MnO	5.19 ± 1.81	1.60 ± 0.44	3.20 ± 1.25	1.71 ± 1.03	MnO	0.12 ± 0.06	0.04 ± 0.03
MgO	1.40 ± 0.19	1.62 ± 0.17	1.06 ± 0.56	1.45 ± 0.43	MgO	0.03 ± 0.01	0.02 ± 0.02
CaO	8.23 ± 0.66	9.50 ± 0.29	8.67 ± 0.54	9.62 ± 0.43	CaO	22.52 ± 0.21	23.06 ± 0.48
Total	101.52 ± 0.22	101.46 ± 0.53	101.00 ± 0.74	100.86 ± 0.84	Total	98.20 ± 0.28	98.18 ± 0.96
Formula 12(O)					Formula 12.5(O)		
Si	2.90 ± 0.02	2.93 ± 0.05	2.88 ± 0.05	2.90 ± 0.04	Si	3.06 ± 0.01	3.05 ± 0.02
Ti	0.02 ± 0.01	0.01 ± 0.01	0.00	0.00	Ti	0.00	0.00
Al	1.98 ± 0.01	2.00 ± 0.01	1.99 ± 0.02	2.00 ± 0.01	Al^{IV}	0.00	0.00
Fe^{2+}	1.72 ± 0.07	1.85 ± 0.04	1.81 ± 0.05	1.82 ± 0.08	Al^{VI}	2.53 ± 0.04	2.51 ± 0.01
Fe^{3+}	0.17 ± 0.05	0.13 ± 0.10	0.25 ± 0.09	0.19 ± 0.08	Fe^{3+}	0.47 ± 0.03	0.48 ± 0.01
Mn	0.35 ± 0.12	0.11 ± 0.03	0.22 ± 0.09	0.12 ± 0.08	Mn	0.01 ± 0.00	0.00
Mg	0.16 ± 0.02	0.19 ± 0.02	0.12 ± 0.06	0.17 ± 0.05	Mg	0.00	0.00

(Continues)

TABLE 1 (Continued)

	Garnet					Epidote	
	Grt_0 (cores) ($N = 2$)	Grt_0 (rims) ($N = 4$)	Grt_I ($N = 5$)	Grt_{II} ($N = 10$)		Ep_0 ($N = 4$)	Ep_{II} ($N = 11$)
Ca	0.69 ± 0.05	0.79 ± 0.02	0.73 ± 0.05	0.80 ± 0.03	Ca	1.86 ± 0.02	1.91 ± 0.04
Total	8.00 ± 0.01	8.00 ± 0.01	8.00 ± 0.01	8.00 ± 0.01	Total	7.94 ± 0.01	7.96 ± 0.02
Sps molar	0.11 ± 0.04	0.03 ± 0.01	0.07 ± 0.03	0.04 ± 0.03			

For the latest stage 2, plagioclase rims (Pl_{II}) and garnet rims (Grt_{II}) were considered, because the equilibrium extends along most grain boundaries, where Pl_{II} and Grt_{II} are observed. Epidote, located along grain boundaries, is also taken into account for the computation of the stage 2 reactive bulk composition. Determining the composition of the equilibration volume of the early stage 1 is more challenging. Due to stage 2 overprinting, only a subset of the stage 1 mineral assemblage volume is preserved and the only remaining information is the composition of minerals. The finite modal proportion of plagioclase and garnet cores (Pl_I and Grt_I) do not necessarily correspond to the effective modal proportion of stage 1. To retrieve the bulk composition of stage 1, a 'relict stage 1' composition was firstly calculated, only taking into account the finite modal abundance and composition of plagioclase core (Pl_I) and garnet core (Grt_I). Stage 2 assemblage is produced after the breakdown of an unknown amount of stage 1 assemblage. The stage 1 reactive composition should lie in between these two end-members, assuming a closed system. To retrieve the proportion of these two end-members and the most likely reactive bulk composition for stage 1, a *T*–*X* phase diagram section (Figure 8) has been computed at a fixed pressure of 0.6 GPa. Composition (*X*) ranges between the 'relict stage 1' composition ($C_{Relict\text{-}Stage1}$) and 'stage 2' composition (C_{Stage2}). The calculated *T*–*X* phase diagram section (Figure 8) has been contoured for grossular and spessartine contents in garnet because they are the most sensitive and robust compositional variables. Figure 8 suggests that preserved Grt_I compositions are consistent with a reactive bulk composition that would consist of a mixture of 70% $C_{Relict\text{-}Stage1}$+30% C_{Stage2}.

4.2 | *P–T* estimations

The *P*–*T* phase diagram section of Figure 9a was computed for the bulk composition of the metamorphic stage 1. The phase relations are very similar to those described by Oliot et al. (2010) for a comparable granodiorite composition. Assemblages consisting of Pl–Qz–Bt±Grt are predicted in the LP–HT part of the diagram ($T > 530$°C). This domain is delimited by the white mica-out boundary, located between ~460°C/0.4 GPa and 600°C/0.65 GPa, and is mainly *P*-dependent. By contrast, the epidote-out limit is far less dependent on pressure, and is located between 480 and 580°C in the pressure range of the diagram. The diagram is divided into two parts by the assemblage boundaries corresponding to the breakdown of Pl into lower temperature Ab–Ep–Wm–Grt±Chl assemblages typical of greenschist facies conditions. These mineralogical changes occur, via low variance

TABLE 2 Local mineral assemblages in the protolith and along the brittle precursor, and phase labelling for magmatic and metamorphic stages

		Protolith		Brittle precursor	
Local assemblages		Qz		Pl–Ep–Wm	
		Pl		Pl–Grt–Py–Ep–Wm	
		Pl+Bt		Pl–Bt–Grt–Ep–Wm–Qz	
		Igneous	**Late magmatic/incipient metamorphic**	**Stage 1**	**Stage 2**
Phase labelling	Biotite	Bt_i	Bt_0	Bt_I	
	Epidote		Ep_0		Ep_{II}
	Garnet		Grt_0	Grt_I	Grt_{II}
	K-feldspar	Kfs			
	Plagioclase	Pl_i	Pl_0	Pl_I	Pl_{II}
	Pyrite			Py	
	Quartz		Qz		
	White mica		Wm		

Cells are coloured in grey when the corresponding phase is not observed. Abbreviations from Whitney and Evans (2010).

TABLE 3 Solid solution models and end-member phases used in the sections

Phases	Solid solution model	Solid solution label	End members	References
Biotite	Bi(W)	Bt	Annite–phlogopite–eastonite	White, Powell, & Johnson (2014)
Chlorite	Chl(W)	Chl	Clinochlore–daphnite–amesite –Al-free chlorite–Fe3-clinochlore	White *et al.* (2014)
Epidote	Ep(HP11)	Ep	Clinozoisite–Fe-epidote	Holland and Powell (2011)
Garnet	Gt(W)	Grt	Almandine–spessartine–pyrope–grossular	White *et al.* (2014)
K-feldspar	San	Kf	Sanidine–albite (high order)	Waldbaum and Thompson (1969)
Plagioclase	Pl(h)	Pl	Anorthite–albite (Ab)	Newton and Haselton (1981)
White mica	Mica(W)	Wm	Muscovite–paragonite–celadonite –Fe3-muscovite–Fe-celadonite	White *et al.* (2014)
Magnetite	mt	Mt		

reactions, in a narrow range between ~440 and 520°C, depending on the pressure. Because of their low variance, these fields are almost independent of bulk composition and therefore constitute very reliable indicators of temperature.

Given that only garnet and plagioclase relicts are preserved and that the full stage 1 mineralogical assemblage is unknown, the *P–T* conditions are only determined based on garnet cores compositions. For the range of pressure and temperature considered, the plagioclase solid solution model of Newton and Haselton (1981) can only model plagioclase compositions with a maximum albite content of ~65%. Above this value, pure albite is predicted. Modelling the measured Pl_I compositions (X_{Ab} = 80–85%) is challenging. For this reason, only the garnet composition is used to constrain the *P–T* conditions of stage 1. The calculated isopleths of the grossular and spessartine contents in garnet suggest that Grt_{II} (X_{Grs} = 0.25–0.27, XSps = 0.06–0.08) was stable at 0.6 ± 0.05 GPa and 500 ± 20°C (red box in Figure 9a). The corresponding stable assemblage is Qz–Grt–Pl–Wm–Chl–Ep±Bt.

The inferred bulk composition of stage 2 has been used to generate the *P–T* pseudosection shown in Figure 9b. Phase relations show a close similarity with those obtained for stage 1, especially on the LT part of the diagram. However, the stability field of biotite in the LP–HT part of the section is reduced at the expense of epidote- and magnetite-bearing assemblages due to the higher proportion of Fe^{3+}/Fe^{2+} in C_{Stage2}. The metamorphic assemblage Qz–Grt–Pl–Ep, with minor biotite and white mica, is predicted to be stable for pressures ranging between 0.7 and 0.8 GPa, assuming temperatures of 500–540°C. Isopleths of albite content in plagioclase and grossular content in garnet rims suggest that Pl_{II} and Grt_{II} (X_{Ab} = 0.60–0.75; X_{Grs} = 0.27–0.30) coexisted at 0.76 ± 0.05 GPa and 520 ± 20°C.

5 | DISCUSSION

5.1 | Plagioclase texture, composition, and zoning: fingerprint of alpine metamorphism and fluid–rock interactions processes

Variation in plagioclase composition is known to reflect changes in *P–T–X* conditions of plagioclase growth and dissolution/precipitation (e.g. Steffen & Selverstone, 2006). Because chemical variation in plagioclase involves a coupled substitution $Ca^{2+}+Al^{3+}=Na^{+}+Si^{4+}$ between albite and anorthite end-members, it is very unlikely that the original growth zoning and compositions can be altered or masked by post-growth intracrystalline diffusion, like in most minerals that involve simple substitutions (e.g. $Fe^{2+}=Mg^{2+}$). The challenge is however to be able to relate the successive compositions to a sequence of processes and geological events. Quantitative compositional maps of plagioclase, shown in Figure 6, revealed at least three distinct generations of plagioclase based on their composition and texture.

The first observed generation of plagioclase (Pl_0) corresponds to relicts of former saussuritized magmatic plagioclase of the host Variscan granodiorite. Saussuritization resulted in an albite-richer composition (ranging from Ab_{72} to Ab_{78}), with numerous euhedral inclusions of epidote and white mica.

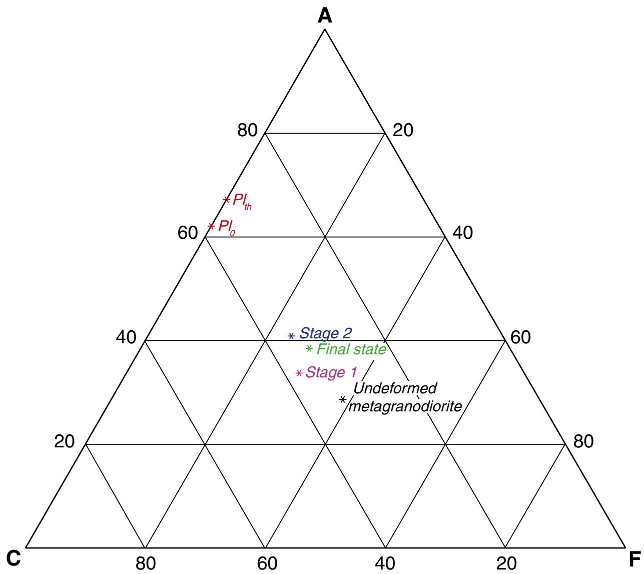

FIGURE 7 ACF ternary diagram showing the different compositions of the garnet-bearing precursor, a theoretical magmatic andesine (Pl_{th}), the saussuritized magmatic plagioclase affected by the brittle precursor (Pl_0), and the undeformed metagranodiorite. A = Al_2O_3–Na_2O–K_2O, C=CaO, and F=FeO+MgO+MnO. Compositions referred to as stages 1 and 2 are used in the calculation of the pseudosections shown in Figure 9a,b, respectively. Final state composition is the bulk composition of the garnet-bearing precursor (composition exported from the whole quantitative map, see Figure 6b,d,e)

Near the brittle precursor, Pl_0 grains are almost completely recrystallized to an aggregate of smaller polygonal plagioclase grains free of inclusions and with a distinct zoning pattern. These grains consist of an oligoclase-rich core (Pl_I) surrounded by an almost continuous rim of andesine plagioclase (Pl_{II}) (e.g. Figure 6b). We suggest that Pl_I is related to alpine regional metamorphism and Pl_{II} is related to a local fluid-induced dissolution–precipitation process.

These microtextures have been successfully numerically modelled by Jessell, Kostenko, and Jamtveit (2003). Using a grain boundary migration algorithm that simulates grain growth driven by reduction in grain boundary energy, Bons and Urai (1992) were able to show that grains undergoing grain growth preserve cores of unreacted material. Although we cannot rule this process out, we rather propose that grain boundary diffusive mass transfer, enhanced by the presence of a fluid phase, is a more likely process to produce the observed plagioclase texture in our studied samples. This process, referred to as pseudomorphic replacement, has been largely described by Putnis and John (2010) and Putnis and Putnis (2007), as an essential mechanism in the re-equilibration of solid phases in the presence of fluids. Since lattice diffusion in plagioclase is very unlikely, we suggest that the chemistry of plagioclase rims (Pl_{II}) reflects the *P–T–X* conditions of fluid percolation. This assumption is supported by the apparent regularity of the compositional zoning throughout the sample suggesting that grain boundary equilibrium was achieved and maintained during plagioclase re-equilibration.

Quantitative compositional mapping of plagioclase (Figure 6a–c) reveals that Pl_{II} formation is not restricted to the brittle precursor (centre of Figure 6a–c) but it extends in the surrounding domains. This suggests that fluid percolation was not restricted to the brittle precursor domain. The distribution of Pl_{II} shows that fluid percolated either along the tortuous grain boundaries network or through larger and more planar fluid pathways (fractures) at high angle to the main precursor (see relative proportions of Pl_{II} on Figure 6a). The extent of fluid percolation perpendicular to the brittle precursor is not quantified. Field observations show that brittle precursors can be surrounded by bleached halos or alteration zones that extend from a few millimetres up to 50 cm (Figure 2g; Pennacchioni & Mancktelow, 2007). Assuming that the macroscopic development of metasomatic haloes is coeval with fluid percolation inferred in this contribution, we suggest that fluid flow was not restricted to the brittle precursor but percolated on either side of it through the host rock via the grain boundary network and microcracks at medium pressure and medium temperature conditions (0.7–0.8 GPa, 510–550°C).

5.2 | Brittle precursor forming conditions and relative timing

A way to constrain the relative timing at which fractures opened is to consider the *P–T* conditions of the assemblage affected by this fracturing. The plagioclase Pl_0 crosscut by the fractures had previously undergone saussuritization. This alteration process results from the hydration of the former magmatic plagioclase (Pl_i). Since this destabilization can be related to cooling, several studies determined the thermal conditions under which it occurs. Que and Allen (1996) claimed that saussuritization occurs between 400 and 600°C, at 150–250 MPa, based on the measurement of fluid inclusions. However, more restricted conditions have been estimated, based on the stability fields of the phases composing the saussuritized assemblage, with temperatures ranging from 250 to 400°C (Deer, Howie, & Zussman, 1992; Drake, Tullborg, & Annersten, 2008; Frey, Capitani, & Liou, 1991; Liou, Kim, & Maruyama, 1983). Other studies suggested that the destabilization of the magmatic plagioclase could also be triggered by changes in *P–T* conditions related to burial (Oliot et al., 2010; Steck, 1976). The plagioclase Pl_0 affected by the fracture could thus have formed either at the end of (or shortly after) magma cooling or during prograde Alpine metamorphism.

Thermodynamic modelling of the garnet-bearing precursor assemblage showed that cores and rims of both garnet and plagioclase are consistent with a continuous prograde path from 0.55–0.65 GPa, 480–520°C to 0.7–0.8 GPa, 510–550°C

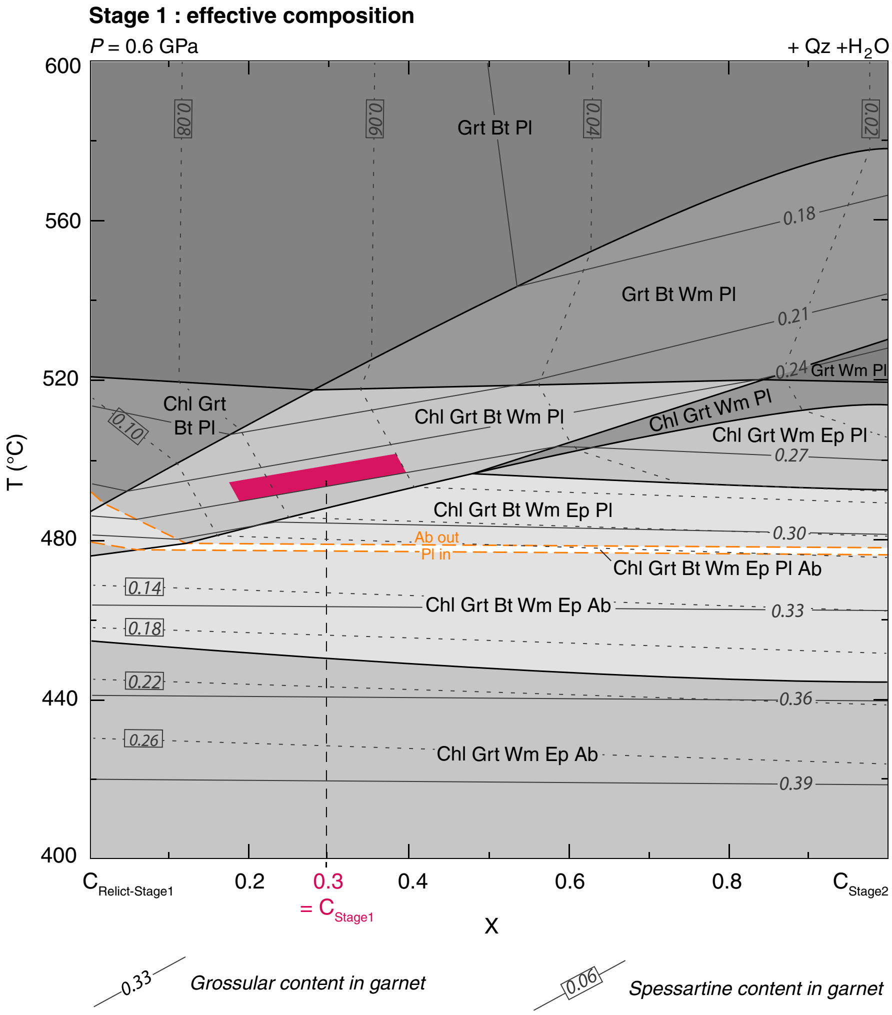

FIGURE 8 *X–T* phase diagram section calculated at $p = 0.6$ GPa. Composition (*X*) ranges between the composition of the relict stage 1 ($C_{Relict\text{-}Stage1}=Grt_I+Pl_I$) and the composition of stage 2 ($C_{Stage2}=Grt_{II}+Pl_{II}+Ep$). Grossular and spessartine contents in garnet are contoured. *X–T* conditions in which Grt_I is stable are highlighted by the red domain. C_{Stage1} is the effective composition estimated for the stage 1

(Figure 9). This means that even in the most immature precursor, no relics of a pre-existing assemblage inherited from lower *P–T* conditions have been preserved. These *P–T* estimates correspond to amphibolite facies conditions (close to the greenshist–amphibolite transition) and are consistent with the conditions of the Alpine ductile deformation in the Neves area (Morteani, 1974). The results of phase equilibria modelling, coupled with petrological observations, indicate that the brittle precursor of the shear zone formed under amphibolite facies conditions.

Previously published structural arguments taken with our petrological observations and thermodynamic model suggest that the brittle deformation and the associated metamorphic fluid flow resulting in shear zones brittle precursors occurred under the same *P–T* conditions as the Alpine ductile deformation in the Neves area. As the Zentralgneise constitutes a low-strain domain, the high-fluid pressure could have produced a network of dilatant joints by brittle failure (Lavier, Bennett, & Duddu, 2013), while the discrete dextral deviatoric component resulted in the observed left-stepping en-échelon geometry. As highlighted by Mancktelow and Pennacchioni (2005), this dextral kinematics inferred from the geometry of the brittle precursors network, along with the dextral kinematics of ductile shear zones, argue for the same kinematic regime for both events.

5.3 | Implications for single ductile shear zone nucleation

Based on detailed field structural analysis, Mancktelow and Pennacchioni (2005) and Pennacchioni and Mancktelow (2007) demonstrated that amphibolite facies ductile shear zones at the Neves area were initiated and developed on a variety of pre-existing planar and rheological boundaries including aplite dykes, bleached haloes surrounding fractures, and the fractures itself. The first two sets of precursors led to the development of characteristic paired shear zone geometry because they nucleated on the edges of the aplite dykes and the bleached haloes, which range in size from a few centimetres to several decimetres (Mancktelow & Pennacchioni, 2005). For the specific case of the bleached haloes, Mancktelow and Pennacchioni (2005) suggested that fluid–rock interactions are responsible for the rheological hardening of this domain and the development of a sufficient

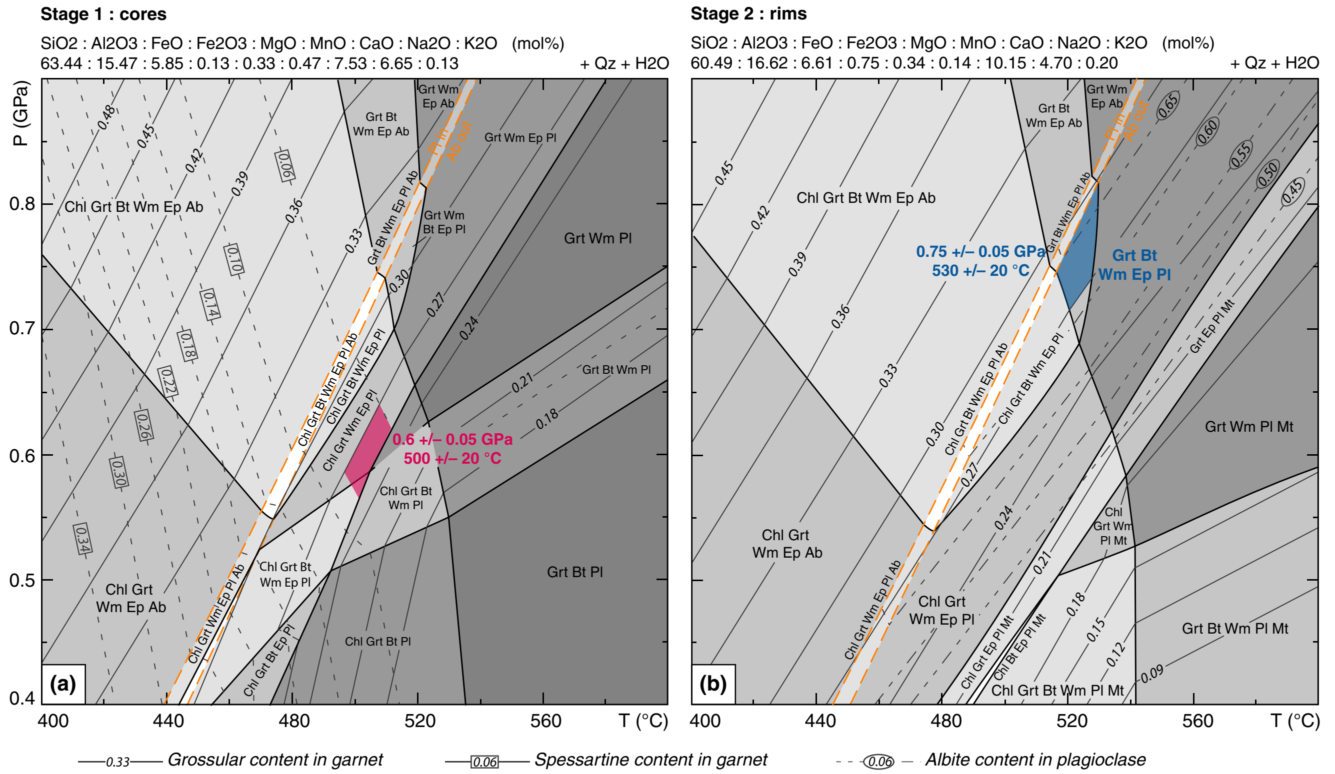

FIGURE 9 *P–T* phase diagram sections calculated (a) for the stage 1 effective composition determined in Figure 8 and (b) for the stage 2 bulk composition. Grossular and spessartine contents in garnet are contoured in (a), grossular content in garnet and albite content in plagioclase are contoured in (b). *P–T* conditions corresponding to the stages 1 (a) and 2 (b) are highlighted by the red and blue domains, respectively

effective viscosity contrast between the coarser grained metasomatic halo and the host metagranodiorite to promote localization of deformation.

In this contribution, we have shown that the brittle precursors are discrete fractures in which minerals grew due to metamorphic fluid–rock interactions. The petrological analysis shows that brittle deformation, metamorphism, and associated fluid flow induced a significant grain size reduction via the recrystallization of saussuritized plagioclase Pl_0 into a fine aggregate of Pl_I and then Pl_{II}. In addition to this major microstructural change, fractures were sealed by the growth of various fine-grained polyphased aggregates of plagioclase, biotite, garnet, quartz, epidote, and pyrite, in various proportions. In contrast to the macroscopic metasomatic haloes, which are rheologically stronger than the surrounding metastable granodiorite, we suggest that the fluid–rock interactions in the immature fractures are responsible for a local weakening.

As shown by Jessell et al. (2004), grain size reduction may thus allow strain localization and, in our case, lead to the formation of single ductile shear zones, broader but controlled, to some extent, by the precursor geometry (Figure 2d–f). This interpretation is consistent with previous field observations of shear zones with preserved biotite-rich straight sutures in their centres (Mancktelow & Pennacchioni, 2005; Pennacchioni & Mancktelow, 2007). Although the brittle deformation is a first-order mechanism for ductile strain localization, we suggest that fluid–rock interactions and more particularly the recrystallization of metastable saussuritized plagioclase (including epidote and white mica inclusions) into a newly formed fine-grained assemblage is also a critical weakening process required to localize deformation in granitic rocks, as already proposed by several authors (e.g. Oliot et al., 2010, 2014).

5.4 | Geological record of slow earthquakes in continental collision setting?

Field observations of concomitant brittle and ductile deformation mechanisms operating in shear zones have led many studies to relate them to the seismic–aseismic cyclicity observed in the middle to lower crust (Behr, Kotowski, & Ashley, 2018; Bernaudin & Gueydan, 2018; Brodsky, Rowe, Meneghini, & Moore, 2009; Fagereng & Sibson, 2010; Hayman & Lavier, 2014; Reber, Hayman, & Lavier, 2014; Rowe & Griffith, 2015; Smith, Collettini, & Holdsworth, 2008). These studies have more specifically linked this rheological behaviour with slow earthquakes, which consist in slow slip events accompanied by non-volcanic tremor and deep low- to very low-frequency earthquakes that have been discovered in a mysterious and key section of faults, corresponding to the transition between the locked seismogenic zone and the deep stable sliding zone (Bernaudin & Gueydan, 2018; Ito, Obara, Shiomi, Sekine, & Hirose, 2007; Nadeau & Dolenc, 2005; Obara, 2002; Obara, Hirose, Yamamizu, & Kasahara, 2004; Rogers & Dragert, 2003; Shelly, Beroza, Ide, & Nakamula, 2006). According to many geophysical studies conducted either in subduction or strike-slip settings, they report that concomitant frictional and viscous deformation occurring at depth-*T* conditions higher than 20 km and 450°C is accompanied by high-fluid pressure conditions (Ito et al., 2007; Katsumata & Kamaya, 2003; Matsubara, Obara, & Kasahara, 2008; Nadeau & Dolenc, 2005; Obara, 2002; Schwartz & Rokosky, 2007; Seno & Yamasaki, 2003; Shelly, Peng, Hill, & Aiken, 2011). Chestler and Creager (2017) also showed that low-frequency earthquakes could result from slips of 0.3–1 mm along surfaces of 80–170 m in length. Finally, frictional–viscous interactions are likely to occur in mixed rheology settings, with low-strain domains surrounded by pervasively foliated matrix (Fagereng & Sibson, 2010).

In this contribution we have demonstrated that the brittle precursors represent the early stage of ductile shear zone development in continental crust and therefore the interplay of concomitant brittle and ductile deformation mechanisms during strain localization at greater than 500°C and depth close to 20 km. Similar brittle–ductile interactions have already been demonstrated by Goncalves et al. (2016) and Wehrens, Berger, Peters, Spillmann, and Herwegh (2016) in continental settings. In these previous studies, including the Neves area, the formation of brittle fractures is associated with fluid percolation that induces either weakening or hardening due to local, and probably rapid, mineralogical and chemical changes. In addition to fluid percolations accompanying the forming of the brittle precursors and the switching towards ductile deformation, high-fluid pressure conditions in the Neves area are also suggested by the presence of numerous quartz veins and metasomatic alteration haloes (Mancktelow & Pennacchioni, 2005; Pennacchioni & Mancktelow, 2007). The Zillertäl massive consists of a km-scale low-strain domain delimited by km-scale shear zones affecting the surrounding metasediments, attesting to the mixed rheology required to generate slow earthquakes (De Vecchi & Mezzacasa, 1986; Glodny et al., 2008; Morteani, 1974; Pennacchioni & Mancktelow, 2007; Steffen & Selverstone, 2006). The length of the brittle precursors in the Neves area, and the quasi-absence of observable offset (Pennacchioni & Mancktelow, 2007) are consistent with the rupture surface and slip associated with low-frequency earthquakes (Chestler & Creager, 2017). To conclude, we speculate that the Neves area contains most of the required conditions (i.e. high temperature brittle/ductile deformation under high-pore fluid pressure in a large-scale mixed rheology) expected to have induced slow earthquakes during Alpine continental collision. If true, then slow earthquakes are not only a geophysical phenomenon related to only subduction zones and strike-slip settings but may also occur in present-day continental collision zones.

6 | CONCLUSIONS

The studied brittle precursor of shear zone attests to Alpine frictional deformation and fluid–rock interactions occurring in a metagranodiorite under assumed viscous regime conditions. We argue that the brittle event producing these discontinuities is more connected to the ductile reactivation than first assumed in the inherited localization model proposed by Mancktelow and Pennacchioni (2005) and Pennacchioni and Mancktelow (2007). Thermodynamic modelling showed that the brittle precursors formed under the same *P–T* conditions than the subsequent ductile shear zones, suggesting the following evolution:

1. Low-strain and high-pore fluid pressure conditions resulting in brittle failure under amphibolite facies conditions.
2. Fracture-controlled syn-kinematic fluid percolation promoting the complete recrystallization of magmatic assemblages.
3. Local decrease in grain size resulting in strain weakening, and in the switching towards a viscous behaviour.

Concomitant brittle and ductile deformation occurring under amphibolite facies conditions, added to high-fluid pressure and low-strain conditions documented in the Zillertäl massive, suggest that the Neves area could have hosted slow earthquakes during Alpine continental collision, supporting the assumption that slow earthquakes could be not restricted to subduction settings.

ACKNOWLEDGEMENTS

The PhD of Thomas Leydier was funded by Ministère de l'Enseignement Supérieur et de la Recherche. We also acknowledge the CNRS INSU TelluS–SYSTER 2016, Observatoire des Sciences de l'Univers Theta Bourgogne – Franche-Comté, program SRO (Soutien à la Recherche de l'Observatoire) 2015, and Ecole Doctorale Environnement-Santé for their financial support. We greatly acknowledge Neil Mancktelow and Giorgio Pennacchioni for introducing us to the Neves area and for the fruitful discussions. We thank Roland, Anna, and Isabella Gruber, the tenants of the Chemnitzer Hütte, for their warm hospitality during the field work. We acknowledge Paul Bons and an anonymous referee for their constructive and helpful comments, and Richard White for his useful suggestions and the editorial handling.

ORCID

Thomas Leydier https://orcid.org/0000-0003-0888-0279
Philippe Goncalves https://orcid.org/0000-0001-8069-7976
Pierre Lanari https://orcid.org/0000-0001-8303-0771
Emilien Oliot https://orcid.org/0000-0002-0370-990X

REFERENCES

Angiboust, S., Kirsch, J., Oncken, O., Glodny, J., Monié, P., & Rybacki, E. (2015). Probing the transition between seismically coupled and decoupled segments along an ancient subduction interface. *Geochemistry, Geophysics, Geosystems*, *16*(6), 1905–1922. https://doi.org/10.1002/2015GC005776

Behr, W. M., Kotowski, A. J., & Ashley, K. T. (2018). Dehydration-induced rheological heterogeneity and the deep tremor source in warm subduction zones. *Geology*, *46*(5), 475–478. https://doi.org/10.1130/G40105.1

Bernaudin, M., & Gueydan, F. (2018). Episodic tremor and slip explained by fluid-enhanced microfracturing and sealing. *Geophysical Research Letters*, *45*(8), 3471–3480. https://doi.org/10.1029/2018GL077586

Bons, P. D., & Urai, J. L. (1992). Syndeformational grain growth: Microstructures and kinetics. *Journal of Structural Geology*, *14*(8), 1101–1109. https://doi.org/10.1016/0191-8141(92)90038-X

Brodsky, E. E., Rowe, C. D., Meneghini, F., & Moore, J. C. (2009). A geological fingerprint of low-viscosity fault fluids mobilized during an earthquake. *Journal of Geophysical Research: Solid Earth*, *114*(B1), https://doi.org/10.1029/2008JB005633

Chestler, S. R., & Creager, K. C. (2017). Evidence for a scale-limited low-frequency earthquake source process. *Journal of Geophysical Research: Solid Earth*, *122*(4), 3099–3114. https://doi.org/10.1002/2016JB013717

Christensen, J. N., Selverstone, J., Rosenfeld, J. L., & DePaolo, D. J. (1994). Correlation by Rb-Sr geochronology of garnet growth histories from different structural levels within the Tauern Window, Eastern Alps. *Contributions to Mineralogy and Petrology*, *118*(1), 1–12. https://doi.org/10.1007/BF00310607

Connolly, J. A. D. (1990). Multivariate phase diagrams: An algorithm based on generalized thermodynamics. *American Journal of Science*, *290*, 666–718. https://doi.org/10.2475/ajs.290.6.666

Connolly, J. A. D. (2005). Computation of phase equilibria by linear programming: A tool for geodynamic modeling and its application to subduction zone decarbonation. *Earth and Planetary Science Letters*, *236*(1), 524–541. https://doi.org/10.1016/j.epsl.2005.04.033

Connolly, J. A. D., & Kerrick, D. M. (1987). An algorithm and computer program for calculating composition phase diagrams. *Calphad*, *11*(1), 1–55. https://doi.org/10.1016/0364-5916(87)90018-6

De Vecchi, G. P., & Mezzacasa, G. (1986). The Pennine basement and cover units in the Mesule group (Southwestern Tauern window). *Memorie Di Scienze Geologiche*, *38*, 365–392.

Deer, W. A., Howie, R. A., & Zussman, J. (1992). *An Introduction to the Rock-Forming Minerals. Sheet Silicates* (2nd ed.). Harlow, Essex/New York, NY: Longman Scientific & Technical.

Drake, H., Tullborg, E.-L., & Annersten, H. (2008). Red-staining of the wall rock and its influence on the reducing capacity around water conducting fractures. *Applied Geochemistry*, *23*(7), 1898–1920. https://doi.org/10.1016/j.apgeochem.2008.02.017

Fagereng, A., & Sibson, R. H. (2010). Melange rheology and seismic style. *Geology*, *38*(8), 751–754. https://doi.org/10.1130/G30868.1

Frey, M., Capitani, C. D., & Liou, J. G. (1991). A new petrogenetic grid for low-grade metabasites. *Journal of Metamorphic Geology*, *9*(4), 497–509. https://doi.org/10.1111/j.1525-1314.1991.tb00542.x

Frisch, W. (1980). Tectonics of the western Tauern window. *Mitteilungen Der Österreichischen Geologischen Gesellschaft*, *71*(72), 65–71.

Fusseis, F., & Handy, M. R. (2008). Micromechanisms of shear zone propagation at the brittle–viscous transition. *Journal of Structural Geology*, *30*(10), 1242–1253. https://doi.org/10.1016/j.jsg.2008.06.005

Glodny, J., Ring, U., & Kühn, A. (2008). Coeval high-pressure metamorphism, thrusting, strike-slip, and extensional shearing in the Tauern Window, Eastern Alps: Tauern Window evolution. *Tectonics*, *27*(4). https://doi.org/10.1029/2007TC002193

Goncalves, P., Oliot, E., Marquer, D., & Connolly, J. A. D. (2012). Role of chemical processes on shear zone formation: An example from the Grimsel metagranodiorite (Aar massif, Central Alps): Shear zone formation. *Journal of Metamorphic Geology*, *30*(7), 703–722. https://doi.org/10.1111/j.1525-1314.2012.00991.x

Goncalves, P., Poilvet, J.-C., Oliot, E., Trap, P., & Marquer, D. (2016). How does shear zone nucleate? An example from the Suretta nappe (Swiss Eastern Alps). *Journal of Structural Geology*, *86*, 166–180. https://doi.org/10.1016/j.jsg.2016.02.015

Guermani, A., & Pennacchioni, G. (1998). Brittle precursors of plastic deformation in a granite: An example from the Mont Blanc massif (Helvetic, western Alps). *Journal of Structural Geology*, *20*(2), 135–148. https://doi.org/10.1016/S0191-8141(97)00080-1

Gueydan, F., Leroy, Y. M., & Jolivet, L. (2001). Grain-size-sensitive flow and shear-stress enhancement at the brittle–ductile transition of the continental crust. *International Journal of Earth Sciences*, *90*(1), 181–196. https://doi.org/10.1007/s005310000160

Hayman, N. W., & Lavier, L. L. (2014). The geologic record of deep episodic tremor and slip. *Geology*, *42*(3), 195–198. https://doi.org/10.1130/G34990.1

Hoernes, S., & Friedrichsen, H. (1974). Oxygen isotope studies on metamorphic rocks of the Western Hohe Tauern area (Austria). *Schweizerische Mineralogische Und Petrographische Mitteilungen*, *54*, 769–788.

Holland, T. J. B., & Powell, R. (2011). An improved and extended internally consistent thermodynamic dataset for phases of petrological interest, involving a new equation of state for solids. *Journal of Metamorphic Geology*, *29*(3), 333–383. https://doi.org/10.1111/j.1525-1314.2010.00923.x

Inger, S., & Cliff, R. A. (1994). Timing of metamorphism in the Tauern Window, Eastern Alps: Rb-Sr ages and fabric formation. *Journal of Metamorphic Geology*, *12*(5), 695–707. https://doi.org/10.1111/j.1525-1314.1994.tb00052.x

Ito, Y., Obara, K., Shiomi, K., Sekine, S., & Hirose, H. (2007). Slow Earthquakes Coincident with Episodic Tremors and Slow Slip Events. *Science*, *315*(5811), 503–506. https://doi.org/10.1126/science.1134454

Jessell, M. W., Bons, P. D., Evans, L., & Piazolo, S. (2004). Numerical experiments into the localization of deformation during recrystallization flow. *Materials Science Forum*, *467*, 647–652. https://doi.org/10.4028/www.scientific.net/MSF.467-470.647

Jessell, M. W., Kostenko, O., & Jamtveit, B. (2003). The preservation potential of microstructures during static grain growth. *Journal of Metamorphic Geology*, *21*(5), 481–491. https://doi.org/10.1046/j.1525-1314.2003.00455.x

Katsumata, A., & Kamaya, N. (2003). Low-frequency continuous tremor around the Moho discontinuity away from volcanoes in the southwest Japan. *Geophysical Research Letters*, *30*(1), 20–1–20–24. https://doi.org/10.1029/2002GL015981

Kurz, W., Neubauer, F., & Genser, J. (1996). Kinematics of Penninic nappes (Glockner Nappe and basement-cover nappes) in the Tauern Window (Eastern Alps, Austria) during subduction and Penninic-Austroalpine collision. *Eclogae Geologicae Helvetiae*, *89*(1), 573–605.

Kurz, W., Neubauer, F., Genser, J., & Dachs, E. (1998). Alpine geodynamic evolution of passive and active continental margin sequences in the Tauern Window (eastern Alps, Austria, Italy): A review. *Geologische Rundschau*, *87*(2), 225–242. https://doi.org/10.1007/s005310050204

Lanari, P., & Engi, M. (2017). Local Bulk Composition Effects on Metamorphic Mineral Assemblages. *Reviews in Mineralogy and Geochemistry*, *83*(1), 55–102. https://doi.org/10.2138/rmg.2017.83.3

Lanari, P., Vho, A., Bovay, T., Airaghi, L., & Centrella, S. (2018). Quantitative compositional mapping of mineral phases by electron probe micro-analyser. *Geological Society, London, Special Publications*, *478*, 39–63. https://doi.org/10.1144/SP478.4

Lanari, P., Vidal, O., De Andrade, V., Dubacq, B., Lewin, E., Grosch, E. G., & Schwartz, S. (2014). XMapTools: A MATLAB-based program for electron microprobe X-ray image processing and geothermobarometry. *Computers & Geosciences*, *62*, 227–240. https://doi.org/10.1016/j.cageo.2013.08.010

Lavier, L., Bennett, R. A., & Duddu, R. (2013). Creep events at the brittle ductile transition: Creep Events at BDT. *Geochemistry, Geophysics, Geosystems*, *14*(9), 3334–3351. https://doi.org/10.1002/ggge.20178

Liou, J. G., Kim, H. S., & Maruyama, S. (1983). Prehnite – Epidote equilibria and their petrologic applications. *Journal of Petrology*, *24*(4), 321–342. https://doi.org/10.1093/petrology/24.4.321

Mancktelow, N. S., & Pennacchioni, G. (2005). The control of precursor brittle fracture and fluid–rock interaction on the development of single and paired ductile shear zones. *Journal of Structural Geology*, *27*(4), 645–661. https://doi.org/10.1016/j.jsg.2004.12.001

Mancktelow, N. S., & Pennacchioni, G. (2013). Late magmatic healed fractures in granitoids and their influence on subsequent solid-state deformation. *Journal of Structural Geology*, *57*, 81–96. https://doi.org/10.1016/j.jsg.2013.09.006.

Matsubara, M., Obara, K., & Kasahara, K. (2008). Three-dimensional P- and S-wave velocity structures beneath the Japan Islands obtained by high-density seismic stations by seismic tomography. *Tectonophysics*, *454*(1–4), 86–103. https://doi.org/10.1016/j.tecto.2008.04.016

Means, W. D. (1984). Shear zones of types I and II and their significance for reconstruction of rock history. *Geological Society of America*, *16*(50) (Abstract. Programs.).

Means, W. D. (1995). Shear zones and rock history. *Tectonophysics*, *247*(1–4), 157–160. https://doi.org/10.1016/0040-1951(95)98214-H

Morteani, G. (1974). Petrology of the Tauern Window, Austrian Alps. *Fortschritte Der Mineralogie*, *52*, 195–220.

Nadeau, R. M., & Dolenc, D. (2005). Nonvolcanic tremors deep beneath the San Andreas Fault. *Science*, *307*(5708), 389–389. https://doi.org/10.1126/science.1107142

Newton, R. C., & Haselton, H. T. (1981). Thermodynamics of the Garnet—Plagioclase—Al2SiO5—Quartz Geobarometer. In R. C. Newton, A. Navrotsky, & B. J. Wood (Eds.), *Thermodynamics of Minerals and Melts* (pp. 131–147). New York, NY: Springer.

Obara, K. (2002). Nonvolcanic deep tremor associated with subduction in southwest Japan. *Science*, *296*(5573), 1679–1681. https://doi.org/10.1126/science.1070378

Obara, K., Hirose, H., Yamamizu, F., & Kasahara, K. (2004). Episodic slow slip events accompanied by non-volcanic tremors in southwest Japan subduction zone. *Geophysical Research Letters*, *31*(23), L23602. https://doi.org/10.1029/2004GL020848

Oliot, E., Goncalves, P., & Marquer, D. (2010). Role of plagioclase and reaction softening in a metagranite shear zone at mid-crustal conditions (Gotthard Massif, Swiss Central Alps). *Journal of Metamorphic Geology*, *28*(8), 849–871. https://doi.org/10.1111/j.1525-1314.2010.00897.x

Oliot, E., Goncalves, P., Schulmann, K., Marquer, D., & Lexa, O. (2014). Mid-crustal shear zone formation in granitic rocks: Constraints from quantitative textural and crystallographic preferred orientations analyses. *Tectonophysics*, *612*, 63–80. https://doi.org/10.1016/j.tecto.2013.11.032

Pennacchioni, G. (2005). Control of the geometry of precursor brittle structures on the type of ductile shear zone in the Adamello tonalites, Southern Alps (Italy). *Journal of Structural Geology*, *27*(4), 627–644. https://doi.org/10.1016/j.jsg.2004.11.008

Pennacchioni, G., & Mancktelow, N. S. (2007). Nucleation and initial growth of a shear zone network within compositionally and structurally heterogeneous granitoids under amphibolite facies conditions. *Journal of Structural Geology*, *29*(11), 1757–1780. https://doi.org/10.1016/j.jsg.2007.06.002

Pennacchioni, G., & Mancktelow, N. S. (2018). Small-scale ductile shear zones: Neither extending, nor thickening, nor narrowing. *Earth-Science Reviews*, *184*, 1–12. https://doi.org/10.1016/j.earscirev.2018.06.004

Putnis, A., & John, T. (2010). Replacement Processes in the Earth's Crust. *Elements*, *6*(3), 159–164. https://doi.org/10.2113/gselements.6.3.159

Putnis, A., & Putnis, C. V. (2007). The mechanism of reequilibration of solids in the presence of a fluid phase. *Journal of Solid State Chemistry*, *180*(5), 1783–1786. https://doi.org/10.1016/j.jssc.2007.03.023

Que, M., & Allen, A. R. (1996). Sericitization of plagioclase in the Rosses Granite Complex, Co. Donegal, Ireland. *Mineralogical Magazine*, *60*(403), 927–936. https://doi.org/10.1180/minmag.1996.060.403.07.

Raith, M. (1971). Seriengliederung und Metamorphose im östlichen Zillertaler Hauptkamm (Tirol, Österreich). *Verh. Geol. BA*, *1*, 163–207.

Raith, M., Raase, P., Kreuzer, H., & Müller, P. (1978). The age of the Alpidic metamorphism in the western Tauern Window, Austrian Alps, accord- ing to radiometric dating. Alps, Apennines, Hellenides, Inter-Union Commission on Geodynamics. *Scientific Reports*, *38*, 140–149.

Reber, J. E., Hayman, N. W., & Lavier, L. L. (2014). Stick-slip and creep behavior in lubricated granular material: Insights into the brittle-ductile transition. *Geophysical Research Letters*, *41*(10), 3471–3477. https://doi.org/10.1002/2014GL059832

Reddy, S. M., Cliff, R. A., & East, R. (1993). Thermal history of the Sonnblick Dome, south-east Tauern Window, Austria: Implications for heterogeneous uplift within the Pennine basement. *Geologische Rundschau*, *82*(4), 667–675. https://doi.org/10.1007/BF00191494

Rogers, G., & Dragert, H. (2003). Episodic Tremor and Slip on the Cascadia Subduction Zone: The Chatter of Silent Slip. *Science*, *300*(5627), 1942–1943. https://doi.org/10.1126/science.1084783

Rowe, C. D., & Griffith, W. A. (2015). Do faults preserve a record of seismic slip: A second opinion. *Journal of Structural Geology*, *78*, 1–26. https://doi.org/10.1016/j.jsg.2015.06.006

Schmid, S. M., Scharf, A., Handy, M. R., & Rosenberg, C. L. (2013). The Tauern Window (Eastern Alps, Austria): A new tectonic map, with cross-sections and a tectonometamorphic synthesis. *Swiss Journal of Geosciences*, *106*(1), 1–32. https://doi.org/10.1007/s00015-013-0123-y

Schwartz, S. Y., & Rokosky, J. M. (2007). Slow slip events and seismic tremor at circum-Pacific subduction zones: Slow slip and seismic tremor. *Reviews of Geophysics*, *45*(3), https://doi.org/10.1029/2006RG000208

Segall, P., & Pollard, D. D. (1983). Joint formation in granitic rock of the Sierra Nevada. *Geological Society of America Bulletin*, *94*, 563–575. https://doi.org/10.1130/0016-7606(1983)94<563:JFIGRO>2.0.CO;2

Segall, P., & Simpson, C. (1986). Nucleation of ductile shear zones on dilatant fractures. *Geology*, *14*, 56–59. https://doi.org/10.1130/0091-7613(1986)14<56:NODSZO>2.0.CO;2

Seno, T., & Yamasaki, T. (2003). Low-frequency tremors, intraslab and interplate earthquakes in Southwest Japan-from a viewpoint of slab dehydration. *Geophysical Research Letters*, *30*(22), https://doi.org/10.1029/2003GL018349

Shelly, D. R., Beroza, G. C., Ide, S., & Nakamula, S. (2006). Low-frequency earthquakes in Shikoku, Japan, and their relationship to episodic tremor and slip. *Nature*, *442*(7099), 188–191. https://doi.org/10.1038/nature04931

Shelly, D. R., Peng, Z., Hill, D. P., & Aiken, C. (2011). Triggered creep as a possible mechanism for delayed dynamic triggering of tremor and earthquakes. *Nature Geoscience*, *4*(6), 384–388. https://doi.org/10.1038/ngeo1141

Simpson, C. (1985). Deformation of granitic rocks across the brittle-ductile transition. *Journal of Structural Geology*, *7*(5), 503–511. https://doi.org/10.1016/0191-8141(85)90023-9

Smith, S. A. F., Collettini, C., & Holdsworth, R. E. (2008). Recognizing the seismic cycle along ancient faults: CO_2-induced fluidization of breccias in the footwall of a sealing low-angle normal fault. *Journal of Structural Geology*, *30*(8), 1034–1046. https://doi.org/10.1016/j.jsg.2008.04.010

Spear, F. S. (1988). Metamorphic fractional crystallization and internal metasomatism by diffusional homogenization of zoned garnets. *Contributions to Mineralogy and Petrology*, *99*(4), 507–517. https://doi.org/10.1007/BF00371941

Steck, A. (1976). Albit-Oligoklas-Mineralgesellschaften der Peristeritlücke aus alpinmetamorphen Granitgneisen des Gotthardmassivs. *Schweizerische Mineralogische Und Petrographische Mitteilungen*, 56.

Steffen, K. J., & Selverstone, J. (2006). Retrieval of P-T information from shear zones: Thermobarometric consequences of changes in plagioclase deformation mechanisms. *Contributions to Mineralogy and Petrology*, *151*(5), 600–614. https://doi.org/10.1007/s00410-006-0073-8

Stüwe, K. (1997). Effective bulk composition changes due to cooling: A model predicting complexities in retrograde reaction textures. *Contributions to Mineralogy and Petrology*, *129*(1), 43–52. https://doi.org/10.1007/s004100050322

Tourigny, G., & Tremblay, A. (1997). Origin and incremental evolution of brittle/ductile shear zones in granitic rocks: Natural examples from the southern Abitibi Belt, Canada. *Journal of Structural Geology*, *19*(1), 15–27. https://doi.org/10.1016/S0191-8141(96)00075-2

Tremblay, A., & Malo, M. (1991). Significance of brittle and plastic fabrics within the Massawippi Lake fault zone, southern Canadian Appalachians. *Journal of Structural Geology*, *13*(9), 1013–1023. https://doi.org/10.1016/0191-8141(91)90053-L

Tullis, J., Dell'Angelo, L. N., & Yund, R. A.(1990). Ductile shear zones from brittle precursors in feldspathic rocks: the possible role of dynamic recrystallization. In A. Duba, W. Durham, J. Handin, & H. Wang(Eds.), *The Brittle-ductile transition: The heard volume* (pp. 67–82). Washington, DC: American Geophysical Union.

Waldbaum, D. R., & Thompson, J. B. (1969). Mixing properties of sanidine crystalline solutions: IV. Phase diagrams from equations of state. *American Mineralogist*, *54*(9–10), 1274–1298.

Wehrens, P., Berger, A., Peters, M., Spillmann, T., & Herwegh, M. (2016). Deformation at the frictional-viscous transition: Evidence for cycles of fluid-assisted embrittlement and ductile deformation in the granitoid crust. *Tectonophysics*, *693*, 66–84. https://doi.org/10.1016/j.tecto.2016.10.022

White, R. W., & Clarke, G. L. (1994). Garnet-forming reactions and recrystallization in high-grade mylonite zones, MacRobertson Land, east Antarctica. *Journal of Metamorphic Geology*, *12*(6), 853–865. https://doi.org/10.1111/j.1525-1314.1994.tb00064.x

White, R. W., Powell, R., & Johnson, T. E. (2014). The effect of Mn on mineral stability in metapelites revisited: New a–x relations for manganese-bearing minerals. *Journal of Metamorphic Geology*, *32*(8), 809–828. https://doi.org/10.1111/jmg.12095.

Whitney, D. L., & Evans, B. W. (2010). Abbreviations for names of rock-forming minerals. *American Mineralogist*, *95*(1), 185–187. https://doi.org/10.2138/am.2010.3371

How to cite this article: Leydier T, Goncalves P, Lanari P, Oliot E. On the petrology of brittle precursors of shear zones – An expression of concomitant brittle deformation and fluid–rock interactions in the 'ductile' continental crust? *J Metamorph Geol*. 2019;37:1129–1149. https://doi.org/10.1111/jmg.12504